

IEEE TRANSACTIONS ON GEOSCIENCE AND REMOTE SENSING

A PUBLICATION OF THE IEEE GEOSCIENCE AND REMOTE SENSING SOCIETY



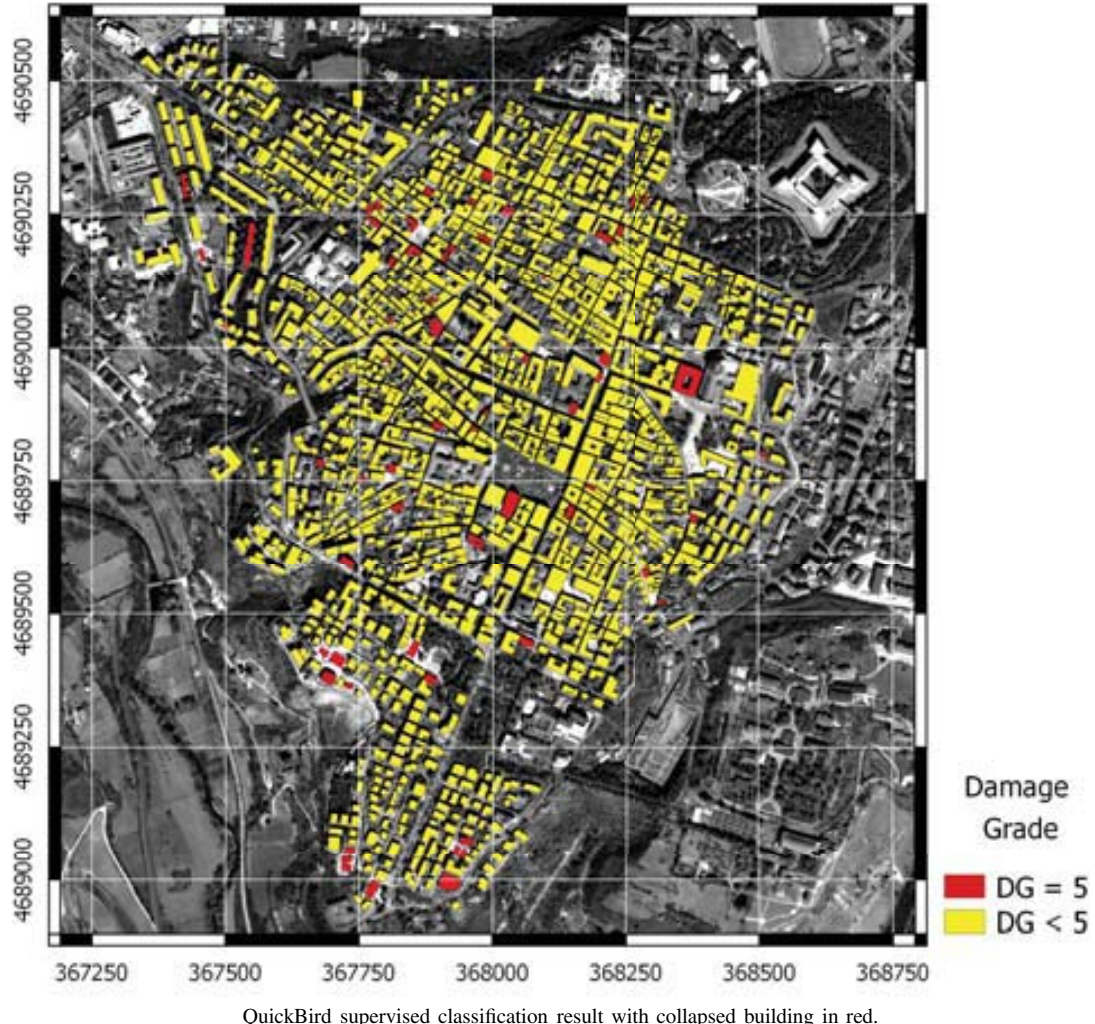
JANUARY 2018

VOLUME 56

NUMBER 1

IGRSD2

(ISSN 0196-2892)



IEEE TRANSACTIONS ON GEOSCIENCE AND REMOTE SENSING

A PUBLICATION OF THE IEEE GEOSCIENCE AND REMOTE SENSING SOCIETY



JANUARY 2018

VOLUME 56

NUMBER 1

IGRSD2

(ISSN 0196-2892)

PAPERS

Sensing Platforms

Validation of Atmospheric Profile Retrievals From the SNPP NOAA-Unique Combined Atmospheric Processing System. Part 1: Temperature and Moisture	N. R. Nalli, A. Gambacorta, Q. Liu, C. D. Barnet, C. Tan, F. Iturbide-Sanchez, T. Reale, B. Sun, M. Wilson, L. Borg, and V. R. Morris	180
A Portable 3-D Imaging FMCW MIMO Radar Demonstrator With a 24×24 Antenna Array for Medium-Range Applications	A. Ganis, E. M. Navarro, B. Schoenlinner, U. Prechtel, A. Meusling, C. Heller, T. Spreng, J. Mietzner, C. Krimmer, B. Haeberle, S. Lutz, M. Loghi, A. Belenguer, H. Esteban, and V. Ziegler	298
Validation of Atmospheric Profile Retrievals from the SNPP NOAA-Unique Combined Atmospheric Processing System. Part 2: Ozone	N. R. Nalli, A. Gambacorta, Q. Liu, C. Tan, F. Iturbide-Sanchez, C. D. Barnet, E. Joseph, V. R. Morris, M. Oyola, and J. W. Smith	598

Methodologies and Applications to:

Oceans and Water

Upwind-Downwind Asymmetry of the Sea Backscattering Normalized Radar Cross Section Versus the Skewness Function	C. Bourlier	17
---	-------------	----

Cryosphere

New CO ₂ Concentration Predictions and Spectral Estimation Applied to the Vostok Ice Core	D. Bonacci and B. Lacaze	145
Iceberg Detection in Open and Ice-Infested Waters Using C-Band Polarimetric Synthetic Aperture Radar	V. Akbari and C. Brekke	407
High-Resolution Interannual Mass Anomalies of the Antarctic Ice Sheet by Combining GRACE Gravimetry and ENVISAT Altimetry	X. Su, C. K. Shum, J. Guo, I. M. Howat, C. Kuo, K. C. Jezek, J. Duan, and Y. Yi	539

Vegetation and Land Surface

Object-Based Superresolution Land-Cover Mapping From Remotely Sensed Imagery	Y. Chen, Y. Ge, G. B. M. Heuvelink, R. An, and Y. Chen	328
Multiobjective Subpixel Land-Cover Mapping	A. Ma, Y. Zhong, D. He, and L. Zhang	422

(Contents Continued on Page 2)

<i>Surface and Subsurface Properties</i>		
Detection of Root Orientation Using Ground-Penetrating Radar	Q. Liu, X. Cui, X. Liu, J. Chen, X. Chen, and X. Cao	93
A Method for Measuring 3-D Surface Deformations With InSAR Based on Strain Model and Variance Component Estimation	J.-H. Liu, J. Hu, Z.-W. Li, J.-J. Zhu, Q. Sun, and J. Gan	239
Triple Collocation to Assess Classification Accuracy Without a Ground Truth in Case of Earthquake Damage Assessment	N. Pierdicca, R. Anniballe, F. Noto, C. Bignami, M. Chini, A. Martinelli, and A. Mannella	485
On Choosing Training and Testing Data for Supervised Algorithms in Ground-Penetrating Radar Data for Buried Threat Detection	D. Reichman, L. M. Collins, and J. M. Malof	497
A Large Comparison of Feature-Based Approaches for Buried Target Classification in Forward-Looking Ground-Penetrating Radar	J. A. Camilo, L. M. Collins, and J. M. Malof	547
<i>Extraterrestrial Sensing</i>		
A Systematic Solution to Multi-Instrument Coregistration of High-Resolution Planetary Images to an Orthorectified Baseline	P. Sidiropoulos and J.-P. Muller	78
Processing, Sensors, and Systems for: Radar Data		
Verification of the Virtual Bandwidth SAR Scheme for Centimetric Resolution Subsurface Imaging From Space	A. Edwards-Smith, K. Morrison, S. Zwieback, and I. Hajnsek	25
A High-Precision Method of Phase-Derived Velocity Measurement and Its Application in Motion Compensation of ISAR Imaging	H. Fan, L. Ren, E. Mao, and Q. Liu	60
Super-Resolution Surface Mapping for Scanning Radar: Inverse Filtering Based on the Fast Iterative Adaptive Approach	Y. Zhang, Y. Zhang, W. Li, Y. Huang, and J. Yang	127
Polarimetric Coherence Pattern: A Visualization and Characterization Tool for PolSAR Data Investigation	S.-W. Chen	286
<i>Synthetic Aperture Radar Data</i>		
Radial Velocity Retrieval for Multichannel SAR Moving Targets With Time–Space Doppler Deambiguity	J. Xu, Z.-Z. Huang, Z.-R. Wang, L. Xiao, X.-G. Xia, and T. Long	35
A Wavelet Decomposition and Polynomial Fitting-Based Method for the Estimation of Time-Varying Residual Motion Error in Airborne Interferometric SAR	H. Q. Fu, J. J. Zhu, C. C. Wang, H. Q. Wang, and R. Zhao	49
Target Reconstruction From Deceptively Jammed Single-Channel SAR	B. Zhao, L. Huang, J. Li, and P. Zhang	152
On the Processing of Very High Resolution Spaceborne SAR Data: A Chirp-Modulated Back Projection Approach	D. Meng, C. Ding, D. Hu, X. Qiu, L. Huang, B. Han, J. Liu, and N. Xu	191
Moving Target Tracking in SAR Data Using Combined Exo- and Endo-Clutter Processing	D. Henke, E. M. Dominguez, D. Small, M. E. Schaepman, and E. Meier	251
Nonlocal Filtering Applied to 3-D Reconstruction of Tomographic SAR Data	O. D'Hondt, C. López-Martínez, S. Guillaso, and O. Hellwich	272
Characteristics Analysis and Image Processing for Full-Polarization Synthetic Aperture Radar Based on Electromagnetic Scattering From Flat Horizontal Perfect Electric Conducting Reflector	S.-X. Zhang, M.-D. Xing, and K. Zhang	313
<i>Hyperspectral Data</i>		
ST-IRGS: A Region-Based Self-Training Algorithm Applied to Hyperspectral Image Classification and Segmentation	F. Li, D. A. Clausi, L. Xu, and A. Wong	3
Atmospheric Correction of Hyperspectral GCAS Airborne Measurements Over the North Atlantic Ocean and Louisiana Shelf	M. Zhang, C. Hu, M. G. Kowalewski, and S. J. Janz	168
Random Forest Ensembles and Extended Multiextinction Profiles for Hyperspectral Image Classification	J. Xia, P. Ghamisi, N. Yokoya, and A. Iwasaki	202
Feature-Driven Active Learning for Hyperspectral Image Classification	C. Liu, L. He, Z. Li, and J. Li	341
Unsupervised Spectral–Spatial Feature Learning via Deep Residual Conv–Deconv Network for Hyperspectral Image Classification	L. Mou, P. Ghamisi, and X. X. Zhu	391
A Two-Phase Multiobjective Sparse Unmixing Approach for Hyperspectral Data	X. Jiang, M. Gong, H. Li, M. Zhang, and J. Li	508

<i>Optical Data</i>		
Learning Multiscale Deep Features for High-Resolution Satellite Image Scene Classification	Q. Liu, R. Hang, H. Song, and Z. Li	117
Optimal Segmentation of High-Resolution Remote Sensing Image by Combining Superpixels With the Minimum Spanning Tree	M. Wang, Z. Dong, Y. Cheng, and D. Li	228
Estimating Error Covariance and Correlation Region in UV Irradiance Data Fusion by Combining TOMS-OMI and UVMRP Ground Observations	Z. Sun, J. Davis, and W. Gao	355
Diversity-Promoting Deep Structural Metric Learning for Remote Sensing Scene Classification	Z. Gong, P. Zhong, Y. Yu, and W. Hu	371
A Novel Image Registration Method Based on Phase Correlation Using Low-Rank Matrix Factorization With Mixture of Gaussian	Y. Dong, T. Long, W. Jiao, G. He, and Z. Zhang	446
Deep Multiple Instance Learning-Based Spatial–Spectral Classification for PAN and MS Imagery	X. Liu, L. Jiao, J. Zhao, J. Zhao, D. Zhang, F. Liu, S. Yang, and X. Tang	461
Relative Geometric Refinement of Patch Images Without Use of Ground Control Points for the Geostationary Optical Satellite GaoFen4	B. Yang, Y. Pi, X. Li, and M. Wang	474
Robust Harris Corner Matching Based on the Quasi-Homography Transform and Self-Adaptive Window for Wide-Baseline Stereo Images	G. Yao, J. Cui, K. Deng, and L. Zhang	559
Active Learning-Based Optimized Training Library Generation for Object-Oriented Image Classification	R. Balasubramaniam, S. Namboodiri, R. R. Nidamanuri, and R. K. S. S. Gorthi	575
<i>Lidar Data</i>		
Determination of Minimum Detectable Deformation of Terrestrial Laser Scanning Based on Error Entropy Model	X. Chen, K. Yu, and H. Wu	105
A Novel Model for Terrain Slope Estimation Using ICESat/GLAS Waveform Data	S. Nie, C. Wang, P. Dong, G. Li, X. Xi, P. Wang, and X. Yang	217
Joint Discriminative Dictionary and Classifier Learning for ALS Point Cloud Classification	Z. Zhang, L. Zhang, Y. Tan, L. Zhang, F. Liu, and R. Zhong	524
<i>Geophysical Data</i>		
Analysis of Electromagnetic Induction for Hydraulic Fracture Diagnostics in Open and Cased Boreholes	J. Dai, Y. Fang, J. Zhou, and Q. H. Liu	264
Joint Inversion of Electromagnetic and Seismic Data Based on Structural Constraints Using Variational Born Iteration Method	T. Lan, H. Liu, N. Liu, J. Li, F. Han, and Q. H. Liu	436
Complex Variational Mode Decomposition for Slope-Preserving Denoising	S. Yu and J. Ma	586

About the Cover: The cover shows the supervised damage detection map at the scale of individual buildings after the destructive earthquake that hit the town of L'Aquila (Central Italy) in 2009. The collapsed buildings, i.e., those characterized by damage grade DG = 5 according to the European Macroseismic Scale 1998 (EMS'98), are highlighted in red. Those with DG < 5 are highlighted in yellow. The map has been derived from a pair of QuickBird images collected before and just after the earthquake, using a supervised image classification trained by a visual inspection. The result has been compared to independent ground surveys carried out after the earthquake by the Department of Civil Protection (DPC) and the National Institute of Geophysics and Volcanology (INGV) using a novel Triple Collocation technique for Classification Assessment (TCCA). The TCCA showed, that assuming a ground survey as the reference for testing, the satellite damage classification can be problematic. The concept of damaged or nondamaged can be controversial on its own, as it may be related to the purpose of the survey and to the conditions in which the teams were operating. The classification, despite some weakness of the satellite data, provided accuracy in distinguishing EMS'96 damage grade 5 comparable to at least one of the surveys. Indeed, the satellite has potentially a more rapid response, and thus may play a role in supporting disaster management. For more information please see "Triple Collocation to Assess Classification Accuracy Without a Ground Truth in Case of Earthquake Damage Assessment," by Pierdicca *et al.*, which begins on page 485.

Target Reconstruction From Deceptively Jammed Single-Channel SAR

Bo Zhao, *Member, IEEE*, Lei Huang, *Senior Member, IEEE*, Jian Li, *Fellow, IEEE*,
and Peichang Zhang, *Member, IEEE*

Abstract—This paper considers the problem of reconstructing true targets in a single-channel synthetic aperture radar (SAR) imaging system, which has been disturbed by deceptive jammings. Since the deceptive jammings are usually confined to the main lobe of an SAR antenna, their time-frequency distributions are different from those of the true echoes. This enables us to utilize a dynamic synthetic aperture (DSA) scheme to extract the characteristics of the true and false targets. Dictionaries about the true and false targets are constructed by taking interactions between scatterers into account. Then a sparsity-driven optimization problem is solved to reconstruct the true and false targets separately with super-resolution. Moreover, the deceptively jammed SAR data are divided into different areas to handle various scenarios efficiently, and strategies for DSA selection are addressed as well. Simulations are provided to verify the effectiveness of the proposed algorithm.

Index Terms—Deceptive jamming, dynamic synthetic aperture (DSA), sparse reconstruction, synthetic aperture radar (SAR).

I. INTRODUCTION

JAMMING suppression is an essential task in synthetic aperture radar (SAR) imaging [1]–[7]. It improves the information acquiring ability of the SAR under complex electromagnetic environments. Unlike conventional jamming schemes, such as radio frequency interferences and barrage jammings, deceptive jammings disturb the SAR information acquisition intentionally and mislead the radar receiver to arrive at wrong decision-making by introducing high-fidelity false targets into SAR imagery [8]–[13]. Therefore, it is a big challenge to tackle the issue of deceptive jammings in SAR imaging.

Manuscript received December 5, 2016; revised April 16, 2017 and July 2, 2017; accepted August 13, 2017. Date of publication September 13, 2017; date of current version December 27, 2017. This work was supported in part by the National Natural Science Foundation of China under Grant U1501253, Grant 61501485, Grant 61501300, Grant 61601300, and Grant 61601304, in part by the China Postdoctoral Science Foundation under Grant 2015M582413 and Grant 2017M610547, in part by the Natural Science Foundation of Guangdong Province, China under Grant 2015A030311030, in part by the Foundation of Shenzhen City under Grant ZDSYS201507081625213, Grant JCYJ20160520165659418, Grant JCYJ20170302142545828, and Grant JCYJ20150324140036835, in part by the Foundation of Nanshan District Shenzhen City under Grant KC2015ZDYF0023A, and in part by Shenzhen University under Grant 201557. (*Corresponding author: Lei Huang*)

B. Zhao, L. Huang, and P. Zhang are with the College of Information Engineering, Shenzhen University, Shenzhen 518060, China (e-mail: dr.lei.huang@ieee.org).

J. Li is with the Electrical and Computer Engineering Department, University of Florida, Gainesville, FL 32611 USA.

Color versions of one or more of the figures in this paper are available online at <http://ieeexplore.ieee.org>.

Digital Object Identifier 10.1109/TGRS.2017.2744178

To improve the information acquisition ability of the SAR against deceptive jammings, various strategies have been suggested in the literature. Multichannel/static SAR, for example, is an effective solution for deceptive jamming suppression. It provides more spatial degrees of freedom (DOFs) than a conventional single-channel SAR. Since the deceptive jammer cannot handle multiple receiving channels simultaneously especially when they work passively, the distinctions between the true echoes and the deceptive jammings in different channels are significant enough for effective deceptive jamming suppression. Using the distinctions, many algorithms have been proposed to suppress the deceptive jammings [14]–[18]. However, they are designed for the complex multichannel/static SAR system but fail to work for the single-channel SAR.

Agile waveform is another effective countermeasure against the deceptive jammings. Various techniques, such as phase-perturbed chirp [19], random initial phase [20], [21], and orthogonal frequency-division multiplexing [22], have been employed to generate agile waveforms. These methods assume that the deceptive jammings cannot be modulated and retransmitted within a single pulse repetition interval. Such an assumption might be true under the current level of technology. Nevertheless, as the real-time performance of a deceptive jammer improves [8], [9], the approaches against deceptive jamming based on agile waveforms can fail to work as well.

This paper aims to develop an effective approach for deceptive jamming suppression based on a single-channel SAR system with a fixed waveform, which is more universal and economical than the multichannel/static SAR approaches and single-channel SAR schemes with agile waveforms. To the best of our knowledge, only Luo *et al.* [23] addressed this issue under such an assumption, but it is for a low-resolution quantized deceptive jammer. As a matter of fact, the low-resolution assumption is not the essence of the problem. And it cannot hold as technology develops, resulting in failure of the algorithm in [23].

The elimination of deceptive jammings for the single-channel fixed-waveform SAR system poses a big challenge, because the available DOFs in space domain (single channel) and time domain (fixed waveform) are quite limited. To handle such a complex problem, we divide it into several subproblems according to different scenarios. In [24], we proposed a differential feature enhancement algorithm using a Doppler frequency filter, leading to an effective identification of the deceptive jammings. For man-made true targets, which convey the important information of SAR imagery, the deceptive jammings are usually well designed with more details [10], [11],

aggravating the difficulty in deceptive jamming identification. In order to cope with this issue, we proposed an introductory concept of dynamic synthetic aperture (DSA) in [25] to reconstruct the deceptively jammed targets using their sparse properties. In the introductory DSA (iDSA) approach, however, a super-resolution preprocessing is required in the azimuth domain to estimate the feasible region before reconstruction, resulting in the dependence of the algorithm performance on the super-resolution estimation results. Moreover, since the optimization problem for the iDSA approach considers only the amplitudes but ignores the phases and the side lobes, the reconstruction result suffers from performance degradation as the scatterers get close. In this paper, the phases and side lobes of the scatterers are considered for dictionary construction, which enables us to obtain a better reconstruction result and achieve super-resolution simultaneously. Furthermore, the multi-DSA approach is used to guarantee the robustness of the proposed algorithm. And various strategies for DSA selection are discussed to handle different situations effectively. As a result, the antideceptive-jamming performance of a conventional SAR system is improved without incurring extra notable expenses. On the other hand, through using the essential differences between SAR echoes and deceptive jammings in the time–frequency domain, the proposed approach is able to work properly even though the deceptive jamming technology improves.

The rest of this paper is organized as follows. Section II presents the signal models of the true echoes and deceptive jammings, and then proposes the reconstruction algorithm using DSA. Section III discusses the parameter selection strategies for different reconstruction purposes. Section IV presents the simulation results. Section V draws the conclusion of this paper.

II. TARGET RECONSTRUCTION FOR SINGLE-CHANNEL SAR

A. Signal Model

Consider an SAR with a single-channel and fixed waveform. To facilitate our discussions, several assumptions are stated as follows.

- 1) No agile waveforms are applied by the SAR. As a result, there is no waveform mismatch between the true echoes and the deceptive jammings.
- 2) Quantization errors of the deceptive jammings are supposed to be small enough. Actually, a digital-to-analog convertor used before deceptive jamming retransmission can perform as a bandpass filter, significantly reducing the quantization errors. Therefore, the quantization errors herein can be ignored in a practical deceptive jammer.
- 3) The accuracy of the deceptive jammings satisfies the azimuth focusing demand; therefore, the slant range modulation errors are required to be smaller than the wavelength, which can be fulfilled by most of the deceptive jamming algorithms [8]–[13]. As a result, the range migration can also be accurately generated due to its greater tolerance to errors at the level of range resolution cell.

- 4) The deceptive jamming modulation algorithm is robust against the motion errors and electronic reconnaissance errors in practical SARs. Such a problem has been addressed in [12] and [13]. This makes the deceptive jammings effective and their mitigation necessary.

These assumptions guarantee that the proposed model is valid even as the deceptive jamming technology advances. Under these conditions, the deceptive jamming modulation is accurate. This makes it impossible to suppress the deceptive jammings in the slant range domain, because the same linear frequency modulation signals are used for both SAR imaging and deceptive jamming. As a result, the necessary imaging procedures, including pulse compression and range migration correction, are assumed to have been carried out in the slant range domain before reconstructing the true and false targets. Furthermore, the super-resolution technique [26]–[28] or windowing process [29] needs to be applied to the pulse compression to suppress the side lobes in the slant range domain. By doing this, the interactions between different slant range resolution cells are reduced and the errors introduced by the adjacent range cells are weakened.

After range processing, the true echo from an arbitrary scatterer has the following form:

$$s(t_r, t_a) = \sigma \operatorname{sinc} \left(B_r \left(t_r - \frac{2R_0}{c} \right) \right) \times a_a(t_a - \tau) \exp \left(-j \frac{4\pi}{\lambda} R(t_a - \tau) \right) \quad (1)$$

where t_r and t_a are the fast and slow times, respectively, σ is the scattering coefficient, B_r is the bandwidth of the SAR signal, c is the propagation velocity of the electromagnetic wave, $a_a(\cdot)$ is the azimuth envelope determined by the antenna directional pattern, τ is the time delay of the scatterer in azimuth, λ is the wavelength, $R(\cdot)$ is the instantaneous slant range history varying with the slow time, and R_0 is the reference range of the scatterer. For simplicity, $a_a(\cdot)$ is considered as an ideal rectangular function in this paper, given by

$$a_a(t_a) = \operatorname{rect} \left(\frac{t_a}{T} \right) = \begin{cases} 1, & |t_a| \leq T/2 \\ 0, & \text{otherwise} \end{cases} \quad (2)$$

where $|\cdot|$ calculates the absolute value and T is the coherent processing interval. If a scatterer falls into the main lobe of the antenna, its echo is considered to be received by the SAR without any attenuation, whereas no echo can be received when the scatterer falls into the side lobes. Such an envelope function is also assumed for the deceptive jammer. As a result, the deceptive jammer can only disturb the SAR from its main lobe. This is the so-called main lobe deceptive jamming. It follows from [8], [10], and [12] that the deceptive jamming is modulated by:

$$s'(t_r, t_a) = \underbrace{\frac{\sigma}{\sigma_J} s_J(t_r, t_a)}_{(a)} * \underbrace{\delta \left(t_r - \frac{2\Delta R(t_a)}{c} \right)}_{(b)} \times \underbrace{\exp \left(-j \frac{4\pi}{\lambda} \Delta R(t_a) \right)}_{(c)} \quad (3)$$

where σ_J is the scattering coefficient of the jammer, $s_J(t_r, t_a)$ is the SAR signal intercepted by the jammer, $*$ is the convolution operator, and $\delta(\cdot)$ is the Dirac delta function. The term (a) in (3) denotes the amplitude scaling, which is usually determined before deceptive jamming starts according to *a priori* knowledge about the true scene. The terms (b) and (c) are the time delay and Doppler phase modulation terms, respectively. Both of them are related to the instantaneous slant range difference between the jammer and the false scatterer. The instantaneous slant range difference can be calculated by $\Delta R(t_a) = R(t_a - \tau) - R_J(t_a)$ with $R_J(t_a)$ being the slant range of the false scatterer to be generated. Assuming that the jammer is located at the origin, the deceptive jammings are only effective in the region $[-T/2, T/2]$ according to (2). Note that the support region of (1) is $[-T/2 - \tau, T/2 - \tau]$, which means that the characteristic of the true instantaneous slant range history has to be extended to $[-T/2, T/2]$ by the jammer according to the detected SAR parameters. As a result, the false scatterer, which appears at the same location as the true one, can be expressed by

$$s'(t_r, t_a) = \sigma' \operatorname{sinc} \left(B_r \left(t_r - \frac{2R_0}{c} \right) \right) \times a_a(t_a) \exp \left(-j \frac{4\pi}{\lambda} R'(t_a - \tau) \right) \quad (4)$$

where σ' and $R'(\cdot)$ are the scattering coefficient and the instantaneous slant range history of the false scatterer, respectively. Note that (1) and (4) possess the same form in the fast time domain. The differences between them are their support regions and Doppler phases. The relationship between the true echo and deceptive jamming is given by

$$s'(t_a) = s(t_a) * \delta(t_a + \tau) \times \exp(-j\pi\tau(2f_{dc} - \gamma\tau + \gamma t_a)). \quad (5)$$

Here, for notational simplicity, we use $s(t_a)$ and $s'(t_a)$ to denote $s(t_r, t_a)$ and $s'(t_r, t_a)$, respectively, f_{dc} is the Doppler frequency center determined by the first-order term of $R(t_a)$, and γ is the Doppler chirp rate determined by the second-order term of $R(t_a)$. Similar to [29], the high-order terms are ignored to simplify the analysis. Denoting the Doppler spectrum of $s(t_a)$ by $S(f_a)$, we have that

$$S'(f_a) = S(f_a - \gamma\tau) \exp(j2\pi f_a \tau) \times \exp(-j\pi(2f_{dc}\tau - \gamma\tau^2)). \quad (6)$$

Compared with the Doppler spectrum of the true scatterer, the spectrum of the false scatterer is shifted along both the slow time and Doppler frequency axes. The first term in (6) shows that the center of the false Doppler spectrum is moved to $\gamma\tau$ on the Doppler frequency axis. The second term of (6), which is a linear phase term about f_a , means that the false Doppler spectrum is shifted by $-\tau$ in the slow time domain. The last exponential term is constant for a certain τ and has no effect on the location of the false Doppler spectrum. The time-frequency distributions of the true echoes and deceptive jammings are shown in Fig. 1.

Although the true echoes of different scatterers distribute in different slow time support regions, their Doppler frequency histories are the same. This leads to a support region with

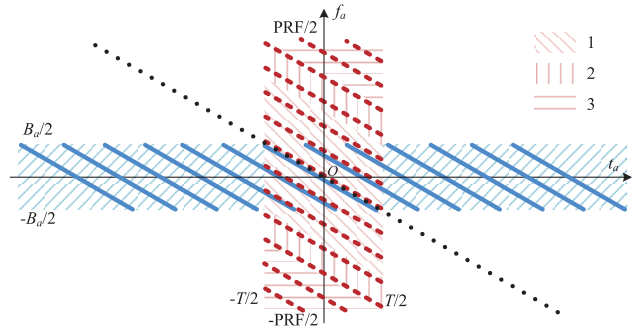


Fig. 1. Time-frequency distributions of the true echoes and deceptive jammings.

B_a width distributing along the slow time axis. The support region of the true echoes is shaded by slashes in Fig. 1. The true echoes are shown by the thick solid lines. Due to the main lobe deceptive jamming assumption, the deceptive jammings lie in region $[-T/2, T/2]$ and distribute along the Doppler frequency axis. The false scatterers, which are shown by thick dashed lines, extend the characteristics of the true scatterers to the jamming support region. The support regions of the true echoes and deceptive jammings overlap totally on each other only when the true and false scatterers lie in the same azimuth cell as the jammer. The farther a scatterer is away from the jammer in azimuth, the fewer public region is shared by the true echoes and deceptive jammings. Note that the deceptive jamming support region is illustrated with different shadows, which are labeled as Regions 1, 2, and 3, respectively. The deceptive jammings in different regions can be dealt with differently due to their distinct effects on the SAR imagery.

Region 1: In this region, the deceptive jammings overlap partly or totally with the true echoes in the time-frequency domain. This makes it difficult to separate the true targets from the false ones. In this paper, we mainly deal with the deceptive jammings in this region. Assume that the deceptive jammings cover an L_J length region in azimuth and denote the length of the synthetic aperture by L . When $L_J \leq 2L$, the false targets fall into Region 1.

Region 2: The deceptive jammings in this region share no common part with the true echoes. Meanwhile, their distributions do not exceed the Doppler frequency support region determined by the pulse repetition frequency (PRF), say $[-\text{PRF}/2, \text{PRF}/2]$. Then, we have $L_J \leq (\beta - 1)L$ with β being the oversampling rate in azimuth. In this region, the deceptive jammings may be effective if they are not removed. However, they can also be easily suppressed by a bandpass filter. Therefore, the effectiveness of deceptive jammings in this region relies on the imaging algorithm.

Region 3: When $L_J > (\beta - 1)L$, the Nyquist sampling rate cannot be satisfied, resulting in aliasing for the deceptive jammings. The deceptive jammings in this region cannot be effectively imaged. Therefore, Region 3 should be avoided when the deceptive jammings are generated.

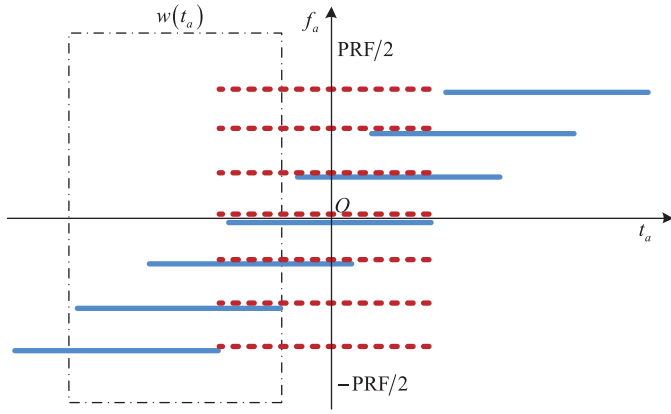


Fig. 2. Time–frequency distributions of the true echoes and deceptive jammings after dechirping.

The oversampling rate β is usually greater than 1 to guarantee the undistorted collection of the SAR echoes. This also provides the space for the deceptive jammings. In the following discussions, $\beta \geq 3$ is assumed so that our discussions can be focused on the elimination of deceptive jammings in Region 1.

B. DSA Processing

The differences between the true and false targets mainly appear in azimuth. In order to easily extract the characteristics of the true and false targets, the dechirping technique is used for azimuth coherent processing. The Doppler frequency center correction (a necessary procedure for squint SAR imaging mode) can also be performed together with dechirping. Therefore, the reference signal is given by

$$s_0(t_a) = \text{rect}\left(\frac{t_a}{T_r}\right) \exp(-j\pi(2f_{\text{dct}}t_a + \gamma t_a^2)) \quad (7)$$

where $T_r = \text{PRF}/\gamma$. The reference signal is shown by the dotted line in Fig. 1. It covers the whole region in which the true echoes and deceptive jammings distribute. By performing dechirping on the mixed data (including both the true echoes and the deceptive jammings) that the SAR receives, the time–frequency distribution in Fig. 2 is obtained.

The differential frequencies between the mixed data and the reference signal are retained after dechirping. Related to the locations of scatterers, the differential frequencies can be projected onto the Doppler frequency axis to obtain the azimuth profiles via the Fourier transform. Although the deceptive jammings distribute within $[-T/2, T/2]$ due to the main lobe deceptive jamming assumption, as shown in Fig. 1, the differential frequencies between the deceptive jammings and the reference signal are the same as those of the true echoes. This leads to the same imaging results of the false targets as the true ones, which is the reason why the deceptive jammings are effective.

For the purpose of deceptive jamming suppression, the characteristics of the true and false scatterers should be totally or partly retained through imaging processing. To extract the characteristics of the true echoes and deceptive jammings,

a DSA $w(t_a)$ is defined as the dashed-dotted line in Fig. 2. It is a data selection window whose expression can be expressed as a rectangular function. That is

$$w(t_a) = \text{rect}\left(\frac{t_a - \eta_w}{T}\right) = \begin{cases} 1, & t_a \in \left[-\frac{T}{2} + \eta_w, \frac{T}{2} + \eta_w\right] \\ 0, & \text{otherwise} \end{cases} \quad (8)$$

where η_w determines the center of the w th DSA. As η_w varies, the DSA moves along the slow time axis, and different parts of the mixed data are extracted. Applying the DSA to the dechirped data, the extracted true echo is

$$\begin{aligned} u(t_a, \eta_w) &= w(t_a)(s(t_a)s_0(t_a)) \\ &= \sigma \text{rect}\left(\frac{t_a - (\eta_w + \tau)/2}{T - |\eta_w - \tau|}\right) \\ &\quad \times \exp(-j2\pi\gamma\tau t_a) \exp(j\phi) \end{aligned} \quad (9)$$

where $\phi = -\pi(4R_0/\lambda + 2f_{\text{dc}}\tau - \gamma\tau^2)$. The deceptive jamming in the DSA is

$$\begin{aligned} u'(t_a, \eta_w) &= w(t_a)(s'(t_a)s_0(t_a)) \\ &= \sigma' \text{rect}\left(\frac{t_a - \eta_w/2}{T - |\eta_w|}\right) \\ &\quad \times \exp(-j2\pi\gamma\tau t_a) \exp(j\phi). \end{aligned} \quad (10)$$

Note that the only difference between (9) and (10) is their support regions determined by the rectangular function. This can also be seen in Fig. 2. Applying the Fourier transform to (9), we have that

$$\begin{aligned} U(f_a, \eta_w) &= \mathcal{F}(u(t_a)) = \sigma \exp(j\phi) \\ &\quad \times \mathcal{F}\left(\text{rect}\left(\frac{t_a - (\eta_w + \tau)/2}{T - |\eta_w - \tau|}\right) \exp(j2\pi\gamma\tau t_a)\right) \\ &= \alpha T \sigma \exp(j\phi) \text{sinc}(\alpha T(f_a + \gamma\tau)) \\ &\quad \times \exp(-j\pi(f_a + \gamma\tau)(\eta_w + \tau)) \end{aligned} \quad (11)$$

where $\mathcal{F}(\cdot)$ denotes the Fourier transform. For a true scatterer in different DSAs, different parts of its true echoes are included, leading to different amplitude attenuations and impulse response width (IRW) extensions, which can be described with a degeneration factor α

$$\alpha = \begin{cases} 1 - \frac{|\eta_w - \tau|}{T}, & \eta_w \in [-T + \tau, T + \tau] \\ 0, & \text{otherwise.} \end{cases} \quad (12)$$

Note that α varies not only with the DSA center η_w but also with the scatterer's location τ . With different values of η_w , different DSAs are formed, leading to a distinct azimuth profile $U(f_a, \eta_w)$. In all the DSAs, the same scatterer can be focused at the same azimuth location $-\gamma\tau$ as a sinc function. Due to the bandwidth loss caused by the DSA, the amplitude of the sinc function decreases and the main lobe expands. For different true scatterers, the amplitude attenuations and IRW extensions in the same DSA are different.

Similarly, the false scatterer in the DSA can be expressed by

$$\begin{aligned} U'(f_a, \eta_w) &= \alpha' T \sigma' \exp(j\phi) \text{sinc}(\alpha' T(f_a + \gamma\tau)) \\ &\quad \times \exp(-j\pi(f_a + \gamma\tau)\eta_w) \exp(j2\pi f_a \tau) \end{aligned} \quad (13)$$

and the degeneration factor of the false scatterer is

$$\alpha' = \begin{cases} 1 - \frac{|\eta_w|}{T}, & \eta_w \in [-T, T] \\ 0, & \text{otherwise.} \end{cases} \quad (14)$$

Note that α' does not vary with τ . This means that different false scatterers in the same DSA have the same amplitude attenuations and IRW extensions. The different characteristics of the true and false scatterers in different DSAs can be used for target reconstruction.

C. Optimization Problem Formulation

The SAR collects the true echoes and deceptive jammings simultaneously. In the sequel, the azimuth profile in the w th DSA can be described by

$$\mathbf{u}_w = \mathbf{G}_w \mathbf{p} + \mathbf{H}_w \mathbf{q} + \boldsymbol{\omega} \quad (15)$$

where $\boldsymbol{\omega}$ is the modeling error and $\mathbf{p}, \mathbf{q} \in \mathbb{C}^N$ are the azimuth profiles of the true and false targets, respectively, defined by

$$\begin{aligned} \mathbf{p} &= [\sigma_1, \sigma_2, \dots, \sigma_N]^T \in \mathbb{C}^N \\ \mathbf{q} &= [\sigma'_1, \sigma'_2, \dots, \sigma'_N]^T \in \mathbb{C}^N. \end{aligned}$$

Equation (15) is a common model, which has been widely used in SAR-related problems for sparse reconstruction by using different dictionaries [5], [6]. In our deceptive jamming problem, $\mathbf{G}_w, \mathbf{H}_w \in \mathbb{C}^{N \times N}$ describe the theoretical azimuth profiles of the true and false scatterers. Their column vectors are, respectively, defined by

$$\mathbf{g}_{wn}^T = \text{asinc}(\alpha T (\mathbf{f}_a^T + \gamma \tau_n)) \odot \exp(-j\pi(\mathbf{f}_a^T + \gamma \tau_n)(\eta_w + \tau_n))$$

$$\begin{aligned} \mathbf{h}_{wn}^T &= \alpha' \text{sinc}(\alpha' T (\mathbf{f}_a^T + \gamma \tau_n)) \odot \exp(-j\pi(\mathbf{f}_a^T + \gamma \tau_n)\eta_w) \\ &\quad \odot \exp(j2\pi\mathbf{f}_a^T \tau_n) \end{aligned}$$

where \mathbf{f}_a is the vectorized Doppler frequency coordinates, τ_n is the time delay of the n th scatterer in azimuth, and \odot is the Hadamard product operator.

In general, we are interested in man-made targets for SAR imagery understanding. These man-made targets are also the focus of deceptive jammings. Constructed with typical structures, such as flats, dihedrals, cylinders, and spheres, man-made targets have strong scattering centers, which are thereby sparse in the observation space. Meanwhile, the false targets are usually constructed with a finite number of discrete scatterers to guarantee the efficiency of deceptive jamming modulation. The false targets, therefore, are sparse in the space domain as well. Due to the sparsity of \mathbf{p} and \mathbf{q} , the target reconstruction problem can be formulated by

$$\begin{aligned} \min_{\mathbf{p}, \mathbf{q}} & \|\mathbf{p}\|_0 + \|\mathbf{q}\|_0 \\ \text{s.t. } & \|\mathbf{G}_w \mathbf{p} + \mathbf{H}_w \mathbf{q} - \mathbf{u}_w\|_2 < \varepsilon \end{aligned} \quad (16)$$

where $\|\cdot\|_2$ is the ℓ_2 -norm and ε denotes a threshold for the reconstruction error. The ℓ_0 -norm counts the number of nonzero elements in the vector. The problem in (16) minimizes the ℓ_0 -norms of \mathbf{p} and \mathbf{q} to obtain the sparsest representations of the true and false target profiles, which also bound the DSA measurement with an acceptable error. The sparsity of

the true and false targets is equally weighted in (16), because effective deceptive jamming usually adopts a power level similar to the SAR echo power [30]. The ℓ_0 -norm problem is well known to be NP-hard [31]. To tackle this issue, the ℓ_0 -norm is usually replaced by a ℓ_1 -norm, tailoring (16) to a computationally feasible problem. That is

$$\begin{aligned} \min_{\mathbf{p}, \mathbf{q}} & \|\mathbf{p}\|_1 + \|\mathbf{q}\|_1 \\ \text{s.t. } & \|\mathbf{G}_w \mathbf{p} + \mathbf{H}_w \mathbf{q} - \mathbf{u}_w\|_2 < \varepsilon. \end{aligned} \quad (17)$$

Converting (17) into an unconstrained optimization problem yields

$$\min_{\mathbf{p}, \mathbf{q}} \|\mathbf{p}\|_1 + \|\mathbf{q}\|_1 + \rho \|\mathbf{G}_w \mathbf{p} + \mathbf{H}_w \mathbf{q} - \mathbf{u}_w\|_2 \quad (18)$$

where ρ is the penalty factor, which, when properly adjusted, leads to a good tradeoff between the sparsity and the reconstruction error. As an amplitude summation of the azimuth profile, the ℓ_1 -norm objective function has the same order of magnitude as the ℓ_2 -norm penalty term, making ρ independent of the coherent processing gain determined by the SAR system. Problem (18) is similar to the morphological component analysis (MCA) [32]. Letting $\mathbf{M}_w = [\mathbf{G}_w, \mathbf{H}_w]$, $\mathbf{z} = [\mathbf{p}; \mathbf{q}]^T$, it follows from (18) that

$$\min_{\mathbf{z}} \|\mathbf{z}\|_1 + \rho \|\mathbf{M}_w \mathbf{z} - \mathbf{u}_w\|_2 \quad (19)$$

which turns out to be the square-root LASSO whose performance is not sensitive to the selection of the penalty factor ρ [33], [34]. Using the CVX toolbox [35], the optimal reconstructions of the true and false profiles are obtained. In particular, by solving (19) for different slant range resolution cells, the imagery of both the true and false targets can be reconstructed.

D. Multiple DSAs Reconstruction Approach

Note that the optimal solution to (19) can be obtained with the DSA, provided that it contains the true echoes and the deceptive jammings. Actually, the reconstruction performance depends on the DSA selection because of the modeling error. Although an optimal DSA, which is discussed in Section III-C, provides effective reconstructions for both the true and false targets, the reconstruction performance cannot always be guaranteed especially when the optimal DSA selection is not available. To improve the robustness of the proposed algorithm, multiple DSAs are used. This, thereby, motivates us to adopt the following optimization problem for reconstruction:

$$\begin{aligned} \min_{\mathbf{p}, \mathbf{q}} & \|\mathbf{p}\|_1 + \|\mathbf{q}\|_1 \\ \text{s.t. } & \|\mathbf{G}_1 \mathbf{p} + \mathbf{H}_1 \mathbf{q} - \mathbf{u}_1\|_2 < \varepsilon \\ & \dots \\ & \|\mathbf{G}_w \mathbf{p} + \mathbf{H}_w \mathbf{q} - \mathbf{u}_w\|_2 < \varepsilon \\ & \dots \\ & \|\mathbf{G}_W \mathbf{p} + \mathbf{H}_W \mathbf{q} - \mathbf{u}_W\|_2 < \varepsilon. \end{aligned} \quad (20)$$

Note that multiple DSAs, which can be selected randomly, are introduced as constraints in (20). According to the definitions, \mathbf{G}_w and \mathbf{H}_w vary with different DSAs.

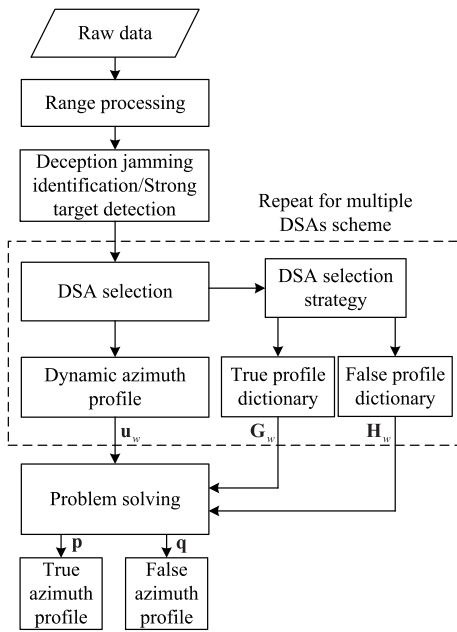


Fig. 3. Flowchart of the proposed algorithm.

By introducing multiple DSAs, the reconstruction result is constrained to fit for different measurements simultaneously. As a result, the multi-DSA scheme is superior to the single-DSA approach in terms of suppressing modeling errors. The constraints can be utilized to transform the cost function into

$$\min_{\mathbf{p}, \mathbf{q}} \|\mathbf{p}\|_1 + \|\mathbf{q}\|_1 + \sum_{w=1}^W \rho_w \|\mathbf{G}_w \mathbf{p} + \mathbf{H}_w \mathbf{q} - \mathbf{u}_w\|_2. \quad (21)$$

Using the similar manipulations adopted in (19), we have that

$$\min_{\mathbf{z}} \|\mathbf{z}\|_1 + \sum_{w=1}^W \rho_w \|\mathbf{M}_w \mathbf{z} - \mathbf{u}_w\|_2. \quad (22)$$

Multiple DSAs are able to provide more observations on the true and false targets to reduce the errors, and thus, the robustness of the proposed algorithm is improved. Nevertheless, the computational cost of the algorithm and the data processing time increase.

The flowchart of the proposed scheme is shown in Fig. 3, and the steps are described as follows.

- 1) Perform range processing, such as pulse compression and range migration correction on the mixed SAR data.
 - 2) Get the coarse SAR imagery via dechirping, and detect the strong targets or identify the deceptive jammings in the SAR imagery. Consequently, the target's location τ and the area needs to be reconstructed are obtained to reduce the computational burden.
 - 3) Select the DSA and calculate the azimuth profile \mathbf{u}_w , the true target description dictionary \mathbf{G}_w , as well as the false target description dictionary \mathbf{H}_w .
 - 4) Repeat steps 3 and 4 to get multiple DSAs for robust reconstruction.
 - 5) Solve the optimization problem to reconstruct the azimuth profiles of the true and false targets.

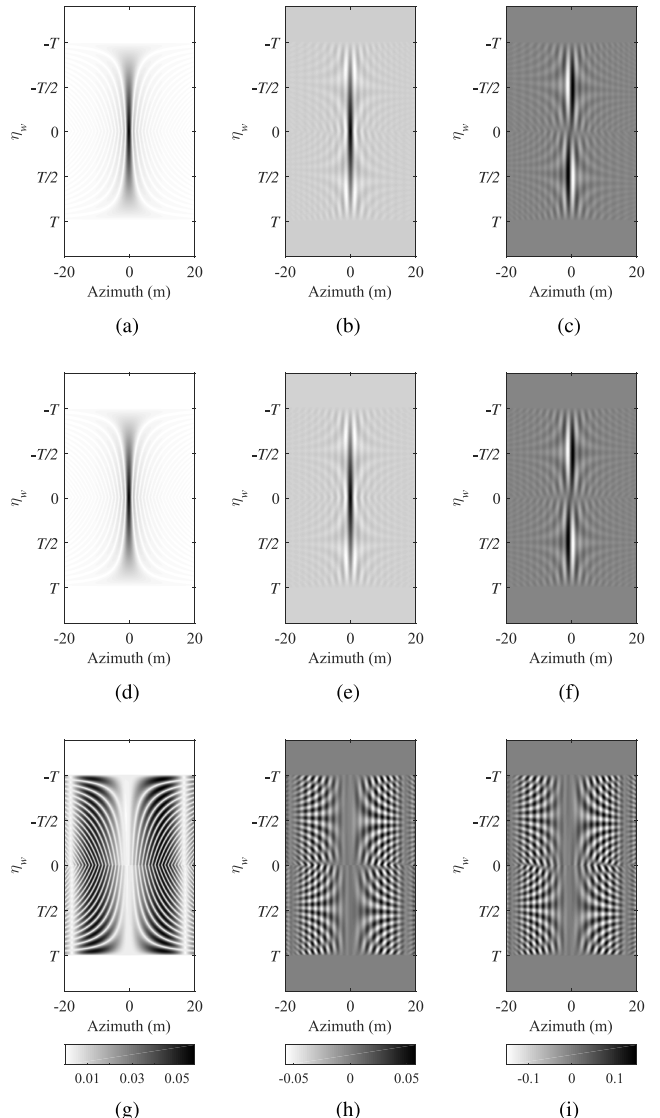


Fig. 4. Modeling errors of true echoes. (a) Amplitude of true echoes. (b) Real component of true echoes. (c) Imaginary component of true echoes. (d) Amplitude of the proposed model. (e) Real component of the proposed model. (f) Imaginary component of the proposed model. (g) Normalized amplitude modeling errors. (h) Normalized real component modeling errors. (i) Normalized imaginary component modeling errors.

Note that steps 3–6 should be performed on each range resolution cell containing the suspicious scatterers to reconstruct the true and false targets.

III DSA SELECTION STRATEGIES

A. Modeling Error

The DSA $w(t_a)$ treats all the true echoes and the deceptive jammings equally. This leads to simple signal models. However, it also introduces errors due to the truncation effect of the rectangular window. As a result, the dictionaries \mathbf{G}_w and \mathbf{H}_w are inaccurate, which degrade the reconstruction performance. Considering a true scatterer, for example, its azimuth profiles in all the available DSAs are organized as an observation matrix and presented in Fig. 4. The amplitudes, and real and imaginary components of the scatterer are shown in Fig. 4(a)–(c), respectively.

Accordingly, the amplitudes, and real and imaginary components of the observation matrix calculated according to the proposed model are given in Fig. 4(d)–(f). Fig. 4(g)–(i) shows the normalized modeling errors. The values of errors are expressed in different gray levels. The errors stay low near the location of the scatterer and become relatively large in the side lobes. More specifically, the maximum errors in the real and imaginary components are 5.81% and 15.11%, respectively, while the maximum amplitude error is 5.79%.

Similarly, the similar level of errors also arises in the deceptive jamming model. Based on 1000 Monte Carlo experiments, the maximum error is about 16.0%, which indicates that the level of modeling errors affects the choice of the DSAs considerably. Therefore, it is necessary to address the issue for DSA selection.

B. Coherence of Dictionaries

The coherence of dictionaries determines the separability of the true and false targets. It can be evaluated by examining the cross correlation between columns of the dictionaries. Denote the continuous expression of \mathbf{g}_{wn}^T and \mathbf{h}_{wn}^T by $g_w(f_a)$ and $h_w(f_a)$, respectively. Then, their cross correlation coefficient is calculated by

$$\begin{aligned} & g_w(f_a) * h_w(f_a) \\ &= g_w^*(-f_a) * h_w(f_a) \\ &= \mathcal{F}^{-1}(\mathcal{F}(g_w(f_a))^* \mathcal{F}(h_w(f_a))) \\ &= \mathcal{F}^{-1}\left(\text{rect}\left(\frac{t_a - (\eta_w + \tau)/2}{T - |\eta_w - \tau|}\right) \text{rect}\left(\frac{t_a - \eta_w/2}{T - |\eta_w|}\right)\right) \\ &= \begin{cases} \mathcal{F}^{-1}\left(\text{rect}\left(\frac{t_a - (\eta_w + \tau)/2}{T - |\eta_w - \tau|}\right)\right), & |\tau| - T < \text{sign}(\tau)\eta_w \leq 0 \\ \mathcal{F}^{-1}\left(\text{rect}\left(\frac{t_a - \tau/2}{T - |\tau|}\right)\right), & 0 < \text{sign}(\tau)\eta_w < |\tau| \\ \mathcal{F}^{-1}\left(\text{rect}\left(\frac{t_a - \eta_w/2}{T - |\eta_w|}\right)\right), & |\tau| \leq \text{sign}(\tau)\eta_w < T \\ 0, & \text{otherwise} \end{cases} \\ &= \mu T \text{sinc}(\mu T(f_a + \gamma \tau)) \end{aligned} \quad (23)$$

where $*$ is the cross correlation operator, $(\cdot)^*$ denotes complex conjugate, \mathcal{F}^{-1} is the inverse Fourier transform, $\text{sign}(\cdot)$ is the sign function, which returns 1 for $\tau \geq 0$ and -1 for $\tau < 0$, and μ is a factor denoting the cross correlation coefficient, given by

$$\mu = \begin{cases} 1 - |\eta_w - \tau|/T, & |\tau| - T < \text{sign}(\tau)\eta_w \leq 0 \\ 1 - |\tau|/T, & 0 < \text{sign}(\tau)\eta_w < |\tau| \\ 1 - |\eta_w|/T, & |\tau| \leq \text{sign}(\tau)\eta_w < T \\ 0, & \text{otherwise.} \end{cases} \quad (24)$$

The maximum of μ is achieved when $0 < \text{sign}(\tau)\eta_w < |\tau|$. Then, we have that

$$\mu_{\max} = 1 - |\tau|/T. \quad (25)$$

It is indicated in (25) that μ_{\max} varies with different azimuth locations as it is a function of τ . When the targets to be reconstructed are located at the same azimuth cell as the deceptive jammer, i.e., $\tau = 0$, we have $\mu_{\max} = 1$. Then the

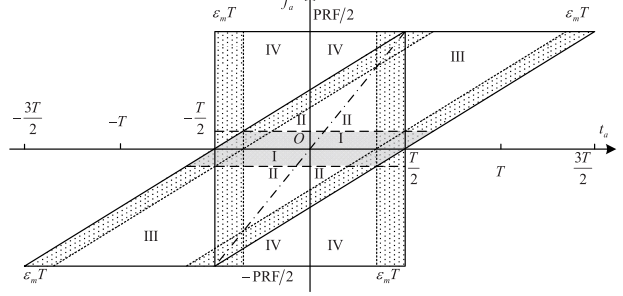


Fig. 5. Effect of modeling errors in different areas.

dictionaries are completely coherent and our algorithm fails. When the targets are located farther away from the jammer in azimuth, μ_{\max} becomes smaller and the dictionaries are less correlated. As a result, the true and false targets can be effectively reconstructed separately.

C. DSA Selection Strategies

As has been revealed in Section III-B that the dictionary coherence increases as the targets get close to the jammer in azimuth, leading to reconstruction performance degradations. To achieve the optimal performance, strategies for DSA selection need be modified according to different locations of the targets. This can be confirmed by the time-frequency distribution of the mixed data shown in Fig. 5.

Due to the amplitude attenuations caused by the DSA, the data at the edges are buried in the modeling errors, which are shaded by dots and appear in the distributions of the true echoes and the deceptive jammings. The DSA, which contains only the edge areas, should be avoided when a DSA is selected. The other areas, labeled as I–IV, contain the true echoes and deceptive jammings in different amounts. As a result, they can be used for different reconstruction strategies according to the locations of the targets. These locations, which can be generally estimated by detecting strong targets or extracted by deceptive jamming identification [24], are assumed to be known. Denoting the azimuth time delay of an arbitrary target center by τ_c , the Areas I–IV can be described as follows.

Area I: When $\tau_c \in [-\varepsilon_m T, \varepsilon_m T]$, the data extracted by the DSA falls into Area I, no matter how η_w is selected. In this area, the characteristic differences between the true and false targets are not obvious because of large μ_{\max} . Moreover, they are further affected by modeling errors. As a result, it is hard to correctly reconstruct the targets in Area I, which is taken as a failure zone.

Area II: When $\tau_c \in [-T, -\varepsilon_m T] \cup [\varepsilon_m T, T]$, Area II is obtained by setting $\eta_w \in [\tau_c + \varepsilon_m T - T, T - \varepsilon_m T]$ for $\tau_c > 0$ or $\eta_w \in [-T + \varepsilon_m T, \tau_c - \varepsilon_m T + T]$ for $\tau_c < 0$. The data in this area contain both the true echoes and deceptive jammings. Therefore, the true and false targets can be reconstructed simultaneously. To improve the effectiveness of the reconstruction, a compromise between the usage of the true echoes and deceptive jammings can be

obtained in this area with $\eta_w = \tau_c/2$, as shown by the dashed-dotted line in Fig. 5. This is referred to as the optimal DSA selection in the following discussion.

Area III: When $\tau_c \in [-T, -\varepsilon_m T] \cup [\varepsilon_m T, T]$, Area III is obtained by using $\eta_w \in [\tau_c - T + \varepsilon_m T, -T] \cup [T, \tau_c + T - \varepsilon_m T]$. Since the data contain only the true echoes, $\mu = 0$ is achieved in this area according to (24). The data in Area III, therefore, can be used to reconstruct the true targets by solving the simplified problem in (19) or (22) with \mathbf{M}_w and \mathbf{z} being replaced by \mathbf{G}_w and \mathbf{p} , respectively.

Area IV: When $\tau_c \in [-T, -\varepsilon_m T] \cup [\varepsilon_m T, T]$, Area IV is obtained by using $\eta_w \in [\tau_c + T, T - \varepsilon_m T] \cup [-T + \varepsilon_m T, \tau_c - T]$. Unlike Area III, the data in this area contain only the deceptive jammings. As a result, the false targets can be reconstructed by solving the simplified problem in (19) or (22), where \mathbf{M}_w and \mathbf{z} are replaced by \mathbf{H}_w and \mathbf{q} , respectively.

Due to the different characteristics of different areas, the DSA selection, say η_w , can be determined according to different reconstruction purposes and the available SAR data. The dictionary \mathbf{H}_w or \mathbf{G}_w can be omitted to simplify the reconstruction problem if data in Area III or IV are used.

IV. NUMERICAL EXAMPLES

In this section, the performance of the proposed DSA algorithm is investigated under various scenarios. Quantitative comparisons are performed against the iDSA algorithm proposed in [25]. To evaluate the performance of target reconstruction, some metrics are defined as follows.

1) *Location Error:* The location errors of the reconstructed scatterers lead to distortions of the targets. This further reduces the quality of the reconstructions. Denote the actual location of the n th scatterer by (x_n, y_n) and the location of the reconstructed scatterer by (\hat{x}_n, \hat{y}_n) . Then the normalized average location error is calculated by

$$\varepsilon_\xi = \frac{1}{\xi N} \sum_{n=1}^N \sqrt{(x_n - \hat{x}_n)^2 + (y_n - \hat{y}_n)^2} \quad (26)$$

where N is the total number of scatterers in a target and ξ is the azimuth resolution of the SAR imagery. Note that when (26) is applied for the false scatterers, additional offsets, which are caused by the deceptive jamming modulation and known as the azimuth positional error, need be compensated in azimuth. The azimuth location of the false scatterer is

$$x'_n = \frac{R_s}{\cos^3 \theta} \frac{R_s \cot \theta - x_n}{\sqrt{(R_s \cot \theta - x_n)^2 + R_s^2}} \quad (27)$$

where θ is the squint angle and R_s is the closest distance between the SAR and the scene center. The derivation of (27) is detailed in the Appendix.

Then the location error evaluation index for the false target is calculated by

$$\varepsilon_\xi = \frac{1}{\xi N} \sum_{n=1}^N \sqrt{(x'_n - \hat{x}_n)^2 + (y_n - \hat{y}_n)^2}. \quad (28)$$

TABLE I
SAR PARAMETERS

Parameter	Value
Bandwidth	300 MHz
Pulse Width	$0.1 \mu s$
Chirp Rate	$3 \times 10^{15} \text{ Hz/s}$
Wavelength	0.03 m
Aperture Length	1 m
Beamwidth	0.03 rad
Closest Range	10 km
Speed	150 m/s
Squint Angle	0°
Doppler Bandwidth	300 Hz
Synthetic Aperture Time	2 s

2) *Residual Power:* Although the reconstructions of the targets can be obtained by solving (19) or (22), some residual power will exist due to the modeling errors, leading to residual scatterers in the reconstruction results. The residual power is calculated by

$$\varepsilon_f = \frac{1}{N_f |E_a|^2} \sum_{n_f=1}^{N_f} |\hat{\sigma}_{n_f}|^2 \quad (29)$$

where $\{\hat{\sigma}_{n_f} \mid |\hat{\sigma}_{n_f}| < \varepsilon'_f\}$ is the power collection of the reconstructed scatterers, which are considered as residual scatterers and ε'_f is a threshold chosen as $1\%|E_a|$ with $|E_a|$ being the average power of the actual scatterers.

3) *Reconstruction Power Error:* The power error of the reconstructed targets is calculated by

$$\varepsilon_e = \frac{\sum_{n=1}^N \|\hat{\sigma}_n\| - |E_n\|^2}{\sum_{n=1}^N |E_n|^2} \quad (30)$$

where $|\hat{\sigma}_n|$ is the amplitude of the n th reconstructed scatterer and $|E_n|$ is the actual amplitude of the n th scatterer.

In practical applications, it is difficult to obtain (x_n, y_n) , E_a , and E_n without *a priori* information. Therefore, these metrics are only used for performance evaluation in the simulations.

A. Reconstruction Using Single DSA

An airborne SAR platform working in the side-looking strip map mode is used in the simulations. The parameters of the SAR platform are listed in Table I.

In Fig. 6, two targets with different locations are encircled by dashed lines and labeled as Targets 1 and 2, respectively. They will be analyzed in the subsequent simulations to study the performance of the proposed algorithm.

According to the SAR parameters, we have $L = 300$ m. The true and false targets distribute uniformly in azimuth with a 15-m distance between adjacent targets and cover a $2L$ -length area. The true targets are arranged in the shape of N, while the false ones are designed in the shape of Z. The imaging result of the true targets without deceptive jammings is given in Fig. 6(a) and the imaging result of the false targets is shown in Fig. 6(b). The scatterers in the true targets are assumed to have the same amplitudes but different phases. The amplitudes of the false scatterers are also

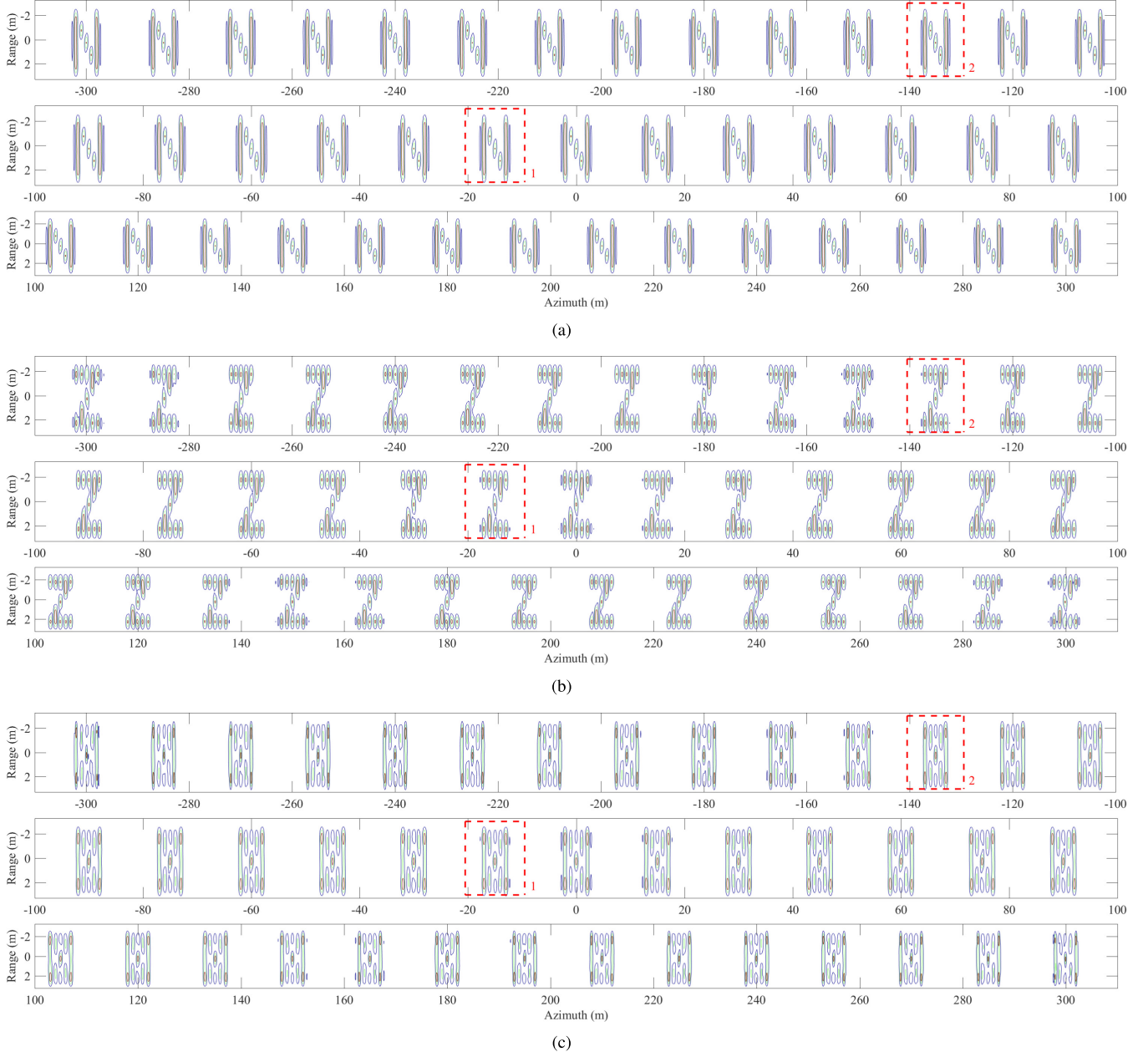


Fig. 6. Target scene settings and deceptive jamming result. (a) True targets. (b) False targets. (c) Deceptive jamming result.

assumed to be the same as the true ones while small random phases are introduced. Denoting the phase of a true scatterer by ψ_t , the phase of the false scatterer at the same location is $\psi_f = \psi_t \pm \psi_{\text{rand}}$, where ψ_{rand} is a random phase ranging from $-\pi/8$ to $\pi/8$. In this way, the false scatterers can be coherently added to the true ones to provide effective jamming, making it hard to recognize the true targets. The deceptively jammed imaging result is shown in Fig. 6(c).

The N-shaped true Target 2 is given in Fig. 7(a). Without the deceptive jammings, the true target can be clearly imaged. When the Z-shaped false target in Fig. 7(b) is introduced by the deceptive jammer, the jammed imaging result is shown in Fig. 7(c). It is seen that the true target cannot be recognized due to the disturbance of the false target.

The optimization problem in (19) can be solved by using only a single DSA. Note that $\rho = 1$ is used to provide an equal consideration of the sparsity and residual errors. The smaller a penalty factor is, the fewer the reconstructed scatterers can be obtained, which are not sufficient to represent the targets. On the contrary, a large penalty factor might lead to residual scatterers, which cannot guarantee an effective suppression of the false target. To show the effect of the DSA selection strategy on the reconstruction, a single DSA is first randomly selected in Area II. The reconstruction results are shown in Fig. 8. It is observed that the true Target 2 is partly reconstructed with some of its scatterers missing, and some strong residual scatterers appear in the reconstruction of the false Target 2. This is caused by the modeling errors.

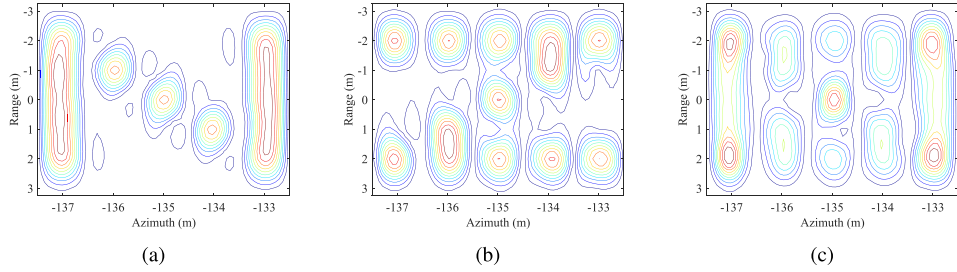


Fig. 7. True and false Targets 2 and deceptive jamming result. (a) True Target 2. (b) False Target 2. (c) Deceptive jamming result.

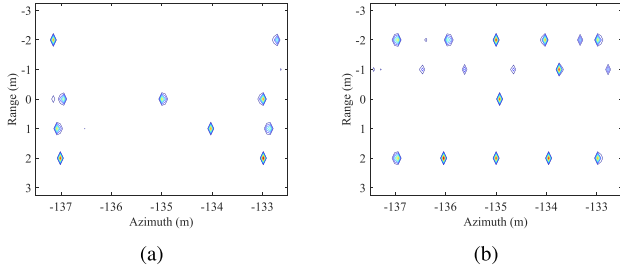


Fig. 8. Reconstruction results using a randomly selected DSA in Area II. (a) Reconstructed true Target 2. (b) Reconstructed false Target 2.

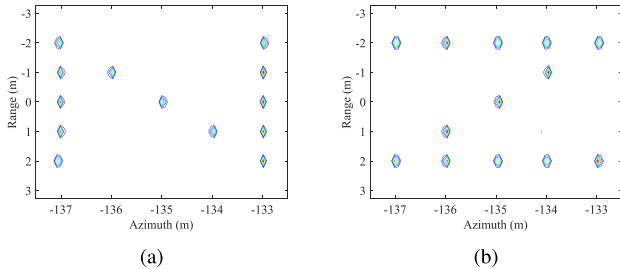


Fig. 9. Reconstruction results using an optimal DSA in Area II. (a) Reconstructed true Target 2. (b) Reconstructed false Target 2.

When the DSA is randomly selected, it is difficult to achieve a good tradeoff between the true echoes and deceptive jammings. As a result, the true and false targets cannot be effectively reconstructed simultaneously.

When the DSA is selected at the optimal location according to the analysis in Section III-C, the reconstruction results of Target 2 are shown in Fig. 9. It is seen in Fig. 9 that the true and false targets are both well reconstructed. Because the sinc-shaped point spread function has been modeled in the description dictionaries \mathbf{G}_w and \mathbf{H}_w , super-resolution is also achieved in the reconstruction results. The evaluation metrics of the reconstructed Target 2 using the random and optimal DSAs are listed in Table II.

It is observed in Table II that the location errors are reduced when the optimal DSA is used. The improvement of the optimal DSA over a random DSA is also observed in the residual power and reconstruction power error of the true Target 2. However, the performance of the false Target 2 degrades when the optimal DSA is used. This is because the randomly selected DSA includes more information of the false target. It should be pointed out that the “optimal” DSA means

TABLE II
EVALUATION METRICS OF RECONSTRUCTION RESULTS OF
TARGET 2 USING THE RANDOM AND OPTIMAL DSAs

Target		ε_ξ (%)	ε_f (%)	ε_e (%)
True Target 2	random DSA	24.57	2.75	29.49
	optimal DSA	2.14	1.69	6.19
False Target 2	random DSA	16.03	3.32	14.30
	optimal DSA	4.27	4.42	15.08

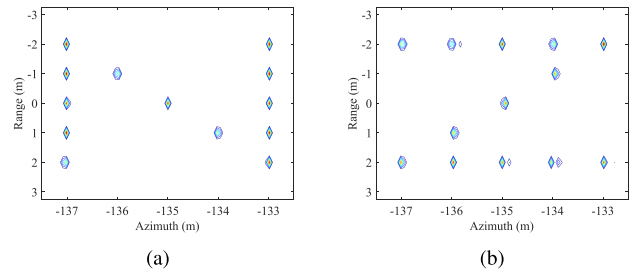


Fig. 10. Reconstruction results of Target 2 using multiple DSA in Area II. (a) True Target 2. (b) False Target 2.

that the DSA is an optimal tradeoff between the true and false targets. Although some amplitude information is lost, the location information enables us to correctly recognize the targets.

B. Reconstruction Using Multiple DSAs

When the optimal DSA is unavailable, (22) provides another solution to the reconstruction problem. The reconstruction errors can be reduced by using multiple observations obtained from different DSAs. In this simulation, we set $W = 20$ and DSAs are randomly selected in Area II. Moreover, ρ_w is set as 1 to make all the constraints be equally considered. Although the residual errors dominate in the multiple DSAs scheme, the residual energy caused by a large penalty factor is smoothed out through the DSAs. As a result, the reconstruction quality can be well guaranteed. The true and false Targets 2 are reconstructed, as shown in Fig. 10.

The error reduction effect leads to the similar reconstruction results to those obtained using the single optimal DSA. Although some weak residual scatterers appear, the reconstructed true and false targets can still be recognized clearly. The reconstruction results of all the targets are given in Fig. 11.

Almost all the targets can be well reconstructed except for those located near the jammer and fall into the failure

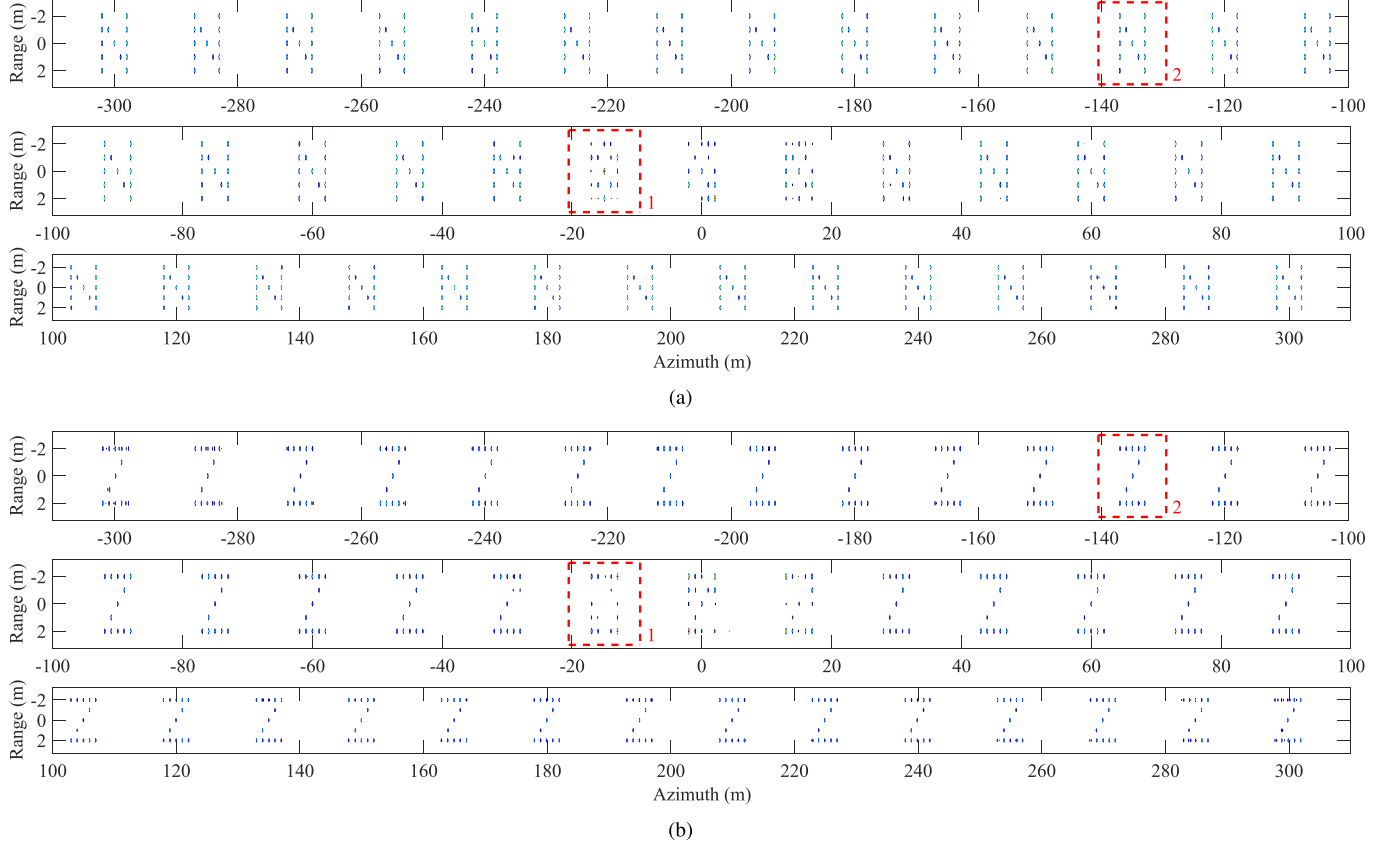


Fig. 11. Reconstruction results using 20 DSAs in Area II. (a) Reconstructed true targets. (b) Reconstructed false targets.

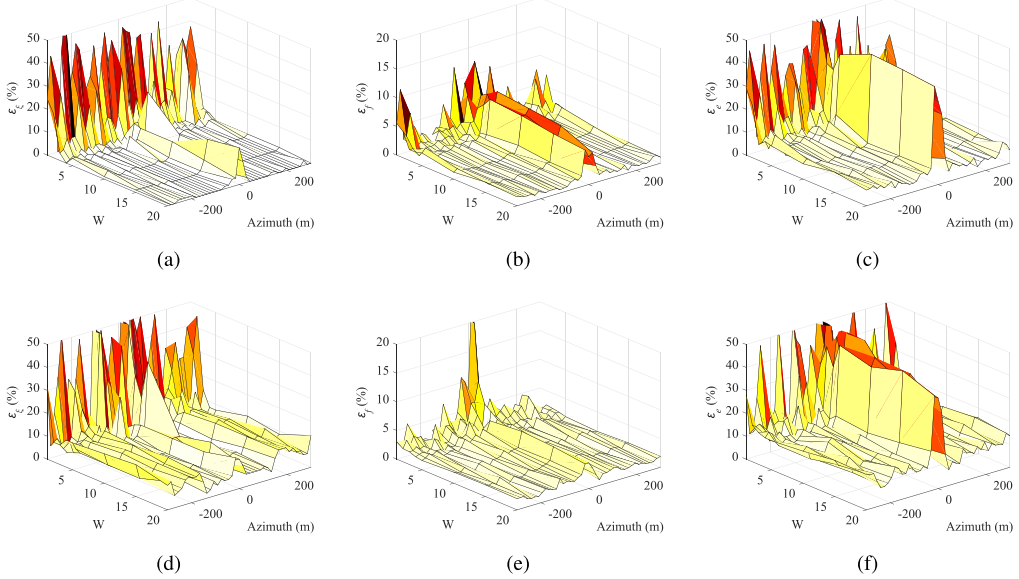


Fig. 12. Evaluation metrics of the reconstruction results using different numbers of DSAs in Area II. (a) Location error of true targets. (b) Residual power of true targets. (c) Reconstruction power error of true targets. (d) Location error of false targets. (e) Residual power of false targets. (f) Reconstruction power error of false targets.

zone. Given in Section III-C, the failure zone is $[-\varepsilon_m L, \varepsilon_m L]$, which corresponds to region $[-48, 48]$ m according to the simulation parameters. As Target 1 falls into the failure zone, it is seriously affected by the modeling errors, leading to the

poor reconstructions that are shown in Fig. 11(a) and (b). Although some of the scatterers can be reconstructed, their locations are totally messed up and the information of the true and false targets is lost. The targets outside the failure

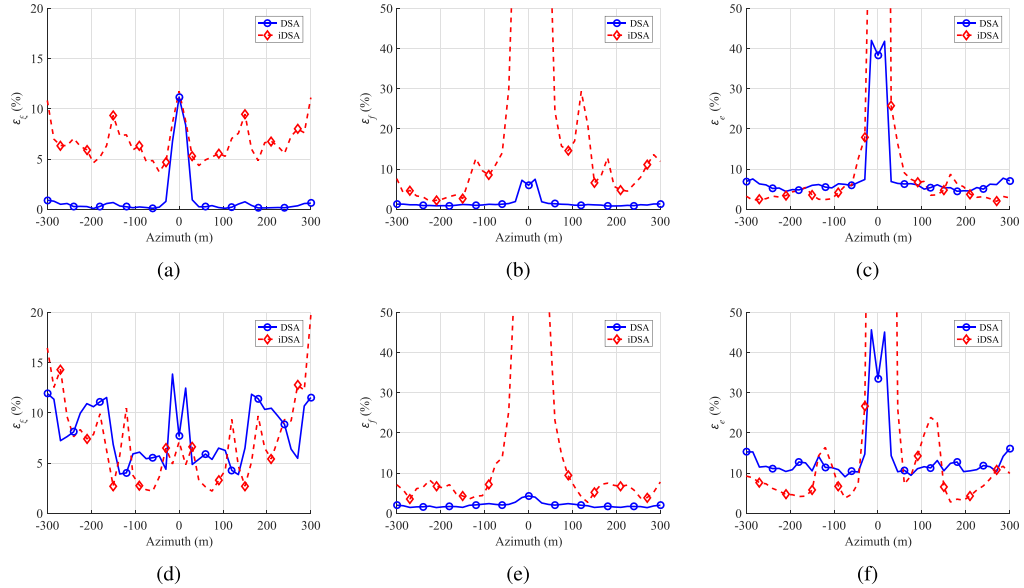


Fig. 13. Evaluation metrics of the reconstruction results using iDSA and DSA algorithms. (a) Location error of true targets. (b) Residual power of true targets. (c) Reconstruction power error of true targets. (d) Location error of false targets. (e) Residual power of false targets. (f) Reconstruction power error of false targets.

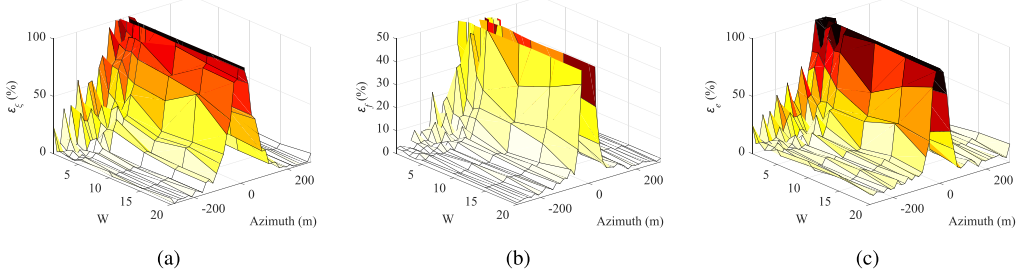


Fig. 14. Evaluation metrics of reconstruction results using different numbers of DSAs in Area III. (a) Location error of true targets. (b) Residual power of true targets. (c) Reconstruction power error of true targets.

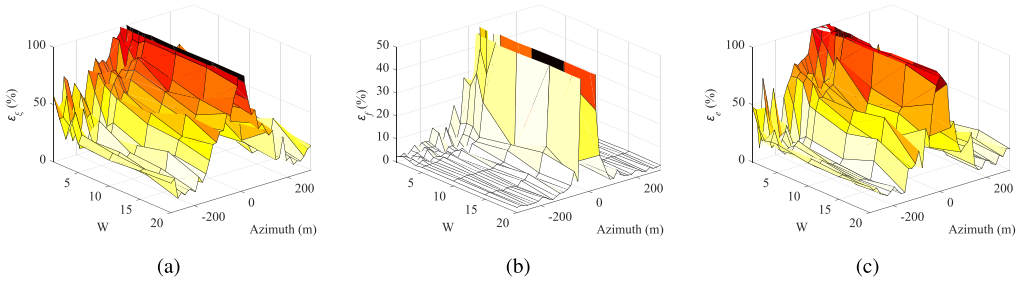


Fig. 15. Evaluation metrics of reconstruction results using different numbers of DSAs in Area IV. (a) Location error of false targets. (b) Residual power of false targets. (c) Reconstruction power error of false targets.

zone can be effectively reconstructed by using the proposed algorithm.

The evaluation metrics of the reconstruction results with different numbers of DSAs are calculated for each target, which are shown in Fig. 12. As the number of DSAs increases, the scatterers can be reconstructed accurately to their actual locations with location errors being smaller than 5%. The residual power is also reduced to less than 5% of the average

power of the true scatterers by using more DSAs, as shown in Fig. 12(b) and (e). Fig. 12(c) and (f) shows the reconstruction power errors of the targets. It is seen that ε_e reduces to about 5% and 10% for the true and false targets, respectively. With the assistance of multiple DSAs, the similar evaluation metrics can be achieved as those obtained using the single optimal DSA, which is provided in Table II. Note that the reconstruction quality improves significantly as the number of

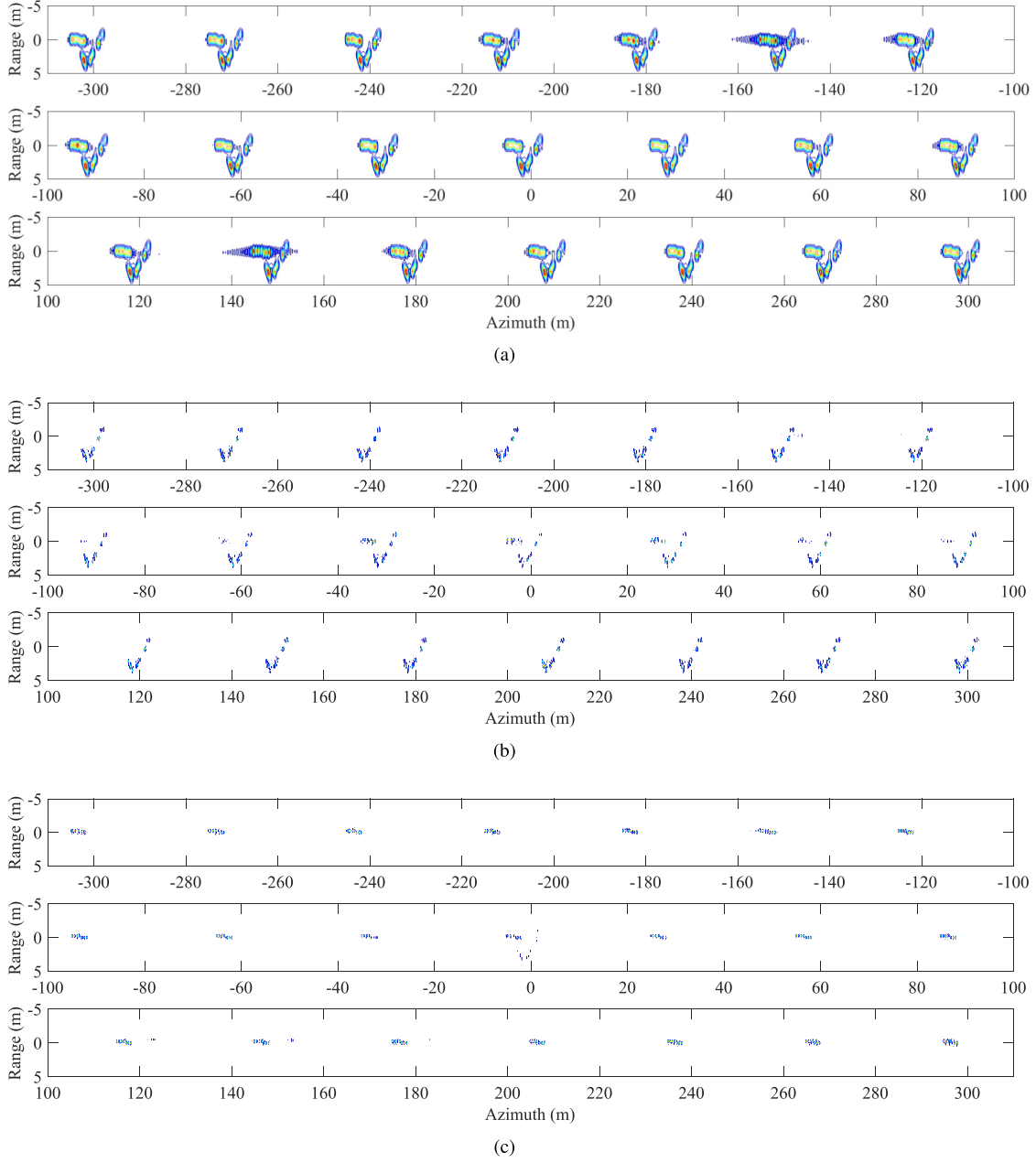


Fig. 16. Reconstruction results of measured targets using 20 DSAs in Area II. (a) Deceptive jamming results of measured targets. (b) Reconstructed true targets. (c) Reconstructed false targets.

DSAs increases from 1 to 5, but a little improvement can be further obtained when more DSAs are used.

Considering the interactions between adjacent scatterers, the proposed algorithm performs better than the iDSA algorithm using the amplitudes of scatterers only. Performing 500 Monte Carlo experiments for the iDSA and DSA algorithms, respectively, we plot the numerical results in Fig. 13.

The iDSA algorithm requires separated super-resolution preprocessing in azimuth before reconstruction, resulting in larger location errors than the DSA algorithm, as indicated in Fig. 13(a). In Fig. 13(d), the location errors of the false targets reconstructed by the DSA algorithm increase to the same level as the iDSA algorithm because of off-grid errors.

Although designed on-grid, the false targets fall into intervals between discrete samples due to the positional errors introduced by deceptive jamming modulation, leading to the off-grid errors. However, the structure of the reconstructed targets can be effectively retained, because the location errors of the reconstructed scatterers are smaller than 15% of a resolution cell. In Fig. 13(b) and (e), the DSA algorithm retains a smaller residual power than the iDSA algorithm by considering the phases and side lobes of the scatterers. For the reconstruction power error, the iDSA algorithm performs better than the DSA algorithm in some area, as shown in Fig. 13(c) and (f). However, unexpected performance degradations occur in the iDSA algorithm, because its

reconstruction performance is strongly related to the separated super-resolution preprocessing. For the DSA algorithm, which performs super-resolution and reconstruction simultaneously, a more stable performance through the whole jammed area and a smaller failure zone, i.e., Area I, can be achieved.

C. Individual Reconstruction Using Data in Areas III and IV

In some practical cases, it is not necessary to simultaneously reconstruct the true and false targets. Therefore, the data in Areas III and IV can be used individually according to the demands of reconstructions and the locations of the targets. When only the true targets are needed, the DSAs can be set just covering the true echoes, say $\eta_w \in [\tau_c + T, T - \varepsilon_m T]$ for $\tau_c > 0$ or $[-T + \varepsilon_m T, \tau_c - T]$ for $\tau_c < 0$. By doing this, the optimization problem is simplified, so that the computation time required for the reconstruction can be reduced. The evaluation metrics are calculated for the reconstruction results using data in Areas III and IV. They are shown in Figs. 14 and 15, respectively. For the data in Areas III and IV, multiple DSAs can lead to improvement for reconstructions. However, it should be noted that the evaluation metrics increase when the targets lie within $\pm L/2$ around the deceptive jammer in azimuth, because only small amounts of data in Areas III or IV are available for reconstructions. As the target locations get farther away from the jammer, the similar reconstruction performance can be achieved as that using data in Area II, which can also be confirmed by the numerical results in Fig. 12.

D. Experiment Using Measured SAR Target Data

In this experiment, the measured true targets are armored personnel carriers provided by the moving and stationary target acquisition and recognition (MSTAR) program [36]. By performing deceptive jamming, a main gun has been added to the body of each target, as shown in Fig. 16(a). Randomly selecting 20 DSAs in Area II, the true and false parts of the targets can be separately reconstructed with super-resolution, which are shown in Fig. 16(b) and (c). It can be observed that in the reconstructed true targets, most of the false guns are removed. For the true targets, which are located near the jammer, the reconstructed false targets in Fig. 16(c) can be used to further reduce the probability of misjudgment.

V. CONCLUSION

In this paper, both the true and false targets are reconstructed by using the single-channel SAR data. Based on the analysis of SAR imaging and deceptive jamming principles, the description dictionaries of the true and false targets are established. Furthermore, the DSA approach is proposed to extract the dynamic characteristics, and an optimization problem is formulated and solved based on the sparsity of the targets. The proposed algorithm is able to operate with a single optimal DSA or achieve a similar performance using multiple randomly selected DSAs. The failure zone caused by the modeling errors is analyzed, and practical strategies are suggested for different reconstruction purposes. Although some residual scatterers appear in the reconstruction results

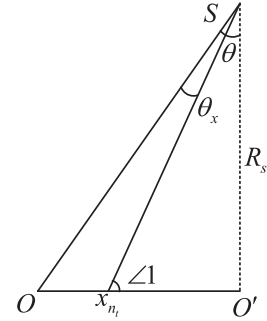


Fig. 17. Geometrical model in the imaging plane.

and the estimated scatterers suffer from power errors, the shape information of the targets can be reconstructed with high fidelity.

APPENDIX AZIMUTH LOCATION OF FALSE SCATTERERS

Based on the main lobe deceptive jamming assumption described in Section II, the shift of the false scatterers in azimuth is realized by converting the time delays into frequency shifts due to the linear correlation between them. As the azimuth distance increases, the error introduced by the linear correlation assumption increases, causing an azimuth positional error. To analyze the azimuth positional error, the geometrical model of the SAR is established in the imaging plane, as shown in Fig. 17.

The point S represents the SAR platform. Without loss of generality, the SAR is assumed to operate in the squint strip map imaging mode with a squint angle θ . The OO' lies in the center of the imaging scene, and R_s is the closest distance between the SAR and OO' . The instantaneous slant range of the origin O is

$$\begin{aligned} R(t_a) &= \sqrt{(vt_a - R_s \tan \theta)^2 + R_s^2} \\ &\approx R_0 - \frac{\lambda}{2} f_{\text{dct}} t_a - \frac{\lambda}{2} \gamma t_a^2. \end{aligned} \quad (\text{A1})$$

Under the accurate deceptive jamming assumption, the false scatterer follows the same instantaneous slant range history but distribute in a different support region from the true scatterer. For the deceptive jamming scheme, $t_a - \tau_x$ is used instead of t_a in (A1). Then, we have that

$$\begin{aligned} R'(t_a - \tau_x) &= R_0 - \frac{\lambda}{2} f_{\text{dct}}(t_a - \tau_x) - \frac{\lambda}{2} \gamma (t_a - \tau_x)^2 \\ &= R(t_a) + \lambda \gamma \tau_x t_a + \frac{\lambda}{2} f_{\text{dct}} \tau_x - \frac{\lambda}{2} \gamma \tau_x^2. \end{aligned} \quad (\text{A2})$$

Besides $R(t_a)$, the linear term about t_a introduces additional Doppler frequency, which causes the azimuth shift of the false scatterer. Taking the n th false scatterer for example, its additional Doppler shift is

$$\begin{aligned} f'_{dx} &= -\frac{2}{\lambda} \frac{d(R(t_a) - R'(t_a - \tau_x))}{dt_a} \\ &= -2\gamma \tau_x = \frac{2v \cos^3 \theta}{\lambda R_s} x'_n \end{aligned} \quad (\text{A3})$$

where x'_n is used to represent its azimuth location with a positional error. It is determined by the deceptive jamming generation. For comparison, the accurate Doppler shift for x_n is derived according to Fig. 17

$$\begin{aligned} f_{dx} &= \frac{2}{\lambda} v \sin(\theta - \theta_x) = \frac{2}{\lambda} v \cos(\angle 1) \\ &= \frac{2v}{\lambda} \frac{R_s \cot \theta - x_n}{\sqrt{(R_s \cot \theta - x_n)^2 + R_s^2}}. \end{aligned} \quad (\text{A4})$$

Letting $f'_{dx} = f_{dx}$, the location of the false scatterer with the positional error can be calculated by

$$x'_n = \frac{R_s}{\cos^3 \theta} \frac{R_s \cot \theta - x_n}{\sqrt{(R_s \cot \theta - x_n)^2 + R_s^2}}. \quad (\text{A5})$$

This means that a false scatterer, which is designed to be at x_n , actually appears at x'_n after deceptive jamming modulation. Therefore, it is x'_n rather than x_n that should be taken as the reference when the location errors of the reconstructed false scatterers are evaluated.

REFERENCES

- [1] V. T. Vu, T. K. Sjogren, M. I. Pettersson, L. Hakansson, A. Gustavsson, and L. M. H. Ulander, "RFI suppression in ultrawideband SAR using an adaptive line enhancer," *IEEE Geosci. Remote Sens. Lett.*, vol. 7, no. 4, pp. 694–698, Oct. 2010.
- [2] Z. Liu, G. Liao, and Z. Yang, "Time variant RFI suppression for SAR using iterative adaptive approach," *IEEE Geosci. Remote Sens. Lett.*, vol. 10, no. 6, pp. 1424–1428, Nov. 2013.
- [3] H. Wang, J. Sun, Y. Wang, and S. Mao, "RFI suppression in SAR based on clutter estimation," in *Proc. IEEE Int. Geosci. Remote Sens. Symp. (IGARSS)*, Melbourne, VIC, Australia, Jul. 2013, pp. 1995–1998.
- [4] S. I. Kelly and M. E. Davies, "RFI suppression and sparse image formation for UWB SAR," in *Proc. 14th Int. Radar Symp. (IRS)*, vol. 2, Dresden, Germany, Jun. 2013, pp. 655–660.
- [5] L. H. Nguyen and T. D. Tran, "Efficient and robust RFI extraction via sparse recovery," *IEEE J. Sel. Topics Appl. Earth Observ. Remote Sens.*, vol. 9, no. 6, pp. 2104–2117, Jun. 2016.
- [6] L. H. Nguyen, T. D. Tran, and T. Do, "Sparse models and sparse recovery for ultra-wideband SAR applications," *IEEE Trans. Aerosp. Electron. Syst.*, vol. 50, no. 2, pp. 940–958, Apr. 2014.
- [7] S. Joy, L. H. Nguyen, and T. D. Tran, "Radio frequency interference suppression in ultra-wideband synthetic aperture radar using range-azimuth sparse and low-rank model," in *Proc. IEEE Radar Conf. (RadarConf)*, Philadelphia, PA, USA, May 2016, pp. 1–4.
- [8] F. Zhou, B. Zhao, M. Tao, X. Bai, B. Chen, and G. Sun, "A large scene deceptive jamming method for space-borne SAR," *IEEE Trans. Geosci. Remote Sens.*, vol. 51, no. 8, pp. 4486–4495, Aug. 2013.
- [9] Y. Liu, W. Wang, X. Pan, Q. Fu, and G. Wang, "Inverse omega-K algorithm for the electromagnetic deception of synthetic aperture radar," *IEEE J. Sel. Topics Appl. Earth Observ. Remote Sens.*, vol. 9, no. 7, pp. 3037–3049, Jul. 2016.
- [10] B. Zhao, F. Zhou, X. Shi, Q. Wu, and B. Zheng, "Multiple targets deception jamming against ISAR using electromagnetic properties," *IEEE Sensors J.*, vol. 15, no. 4, pp. 2031–2038, Apr. 2015.
- [11] X. R. Shi, F. Zhou, B. Zhao, M. L. Tao, and Z. J. Zhang, "Deception jamming method based on micro-Doppler effect for vehicle target," *IET Radar, Sonar Navigat.*, vol. 10, no. 6, pp. 1071–1079, 2016.
- [12] B. Zhao, F. Zhou, and Z. Bao, "Deception jamming for squint SAR based on multiple receivers," *IEEE J. Sel. Topics Appl. Earth Observ. Remote Sens.*, vol. 8, no. 8, pp. 3988–3998, Aug. 2015.
- [13] B. Zhao, L. Huang, F. Zhou, and J. Zhang, "Performance improvement of deception jamming against SAR based on minimum condition number," *IEEE J. Sel. Topics Appl. Earth Observ. Remote Sens.*, vol. 10, no. 3, pp. 1039–1055, Mar. 2017.
- [14] C. Li, "The detection of deception jamming against SAR based on dual-aperture antenna cross-track interferometry," in *Proc. CIE Int. Conf. Radar (CIE ICR)*, Shanghai, China, 2006, pp. 1–4.
- [15] J. Qin, J. Yang, Z. He, and C. Cai, "Analysis of target loss due to suppressing SAR jamming using dual-channel cancellation," in *Proc. CIE Int. Conf. Radar (CIE ICR)*, Shanghai, China, 2006, pp. 1–4.
- [16] B. Z. Sun and J. W. Li, "A new interference elimination method for multi-satellite SAR system," in *Proc. IEEE Int. Geosci. Remote Sens. Symp. (IGARSS)*, Boston, MA, USA, Jul. 2008, pp. IV-1316–IV-1319.
- [17] W. Xiong, G. Zhang, F. Wen, and Y. Zhang, "Trilinear decomposition-based spatial-polarisation filter method for deception jamming suppression of radar," *IET Radar, Sonar Navigat.*, vol. 10, no. 4, pp. 765–773, 2016.
- [18] B. Wang, G. Cui, S. Zhang, B. Sheng, L. Kong, and D. Ran, "Deceptive jamming suppression based on coherent cancelling in multistatic radar system," in *Proc. IEEE Radar Conf. (RadarConf)*, Philadelphia, PA, USA, May 2016, pp. 1–5.
- [19] M. Soumekh, "SAR-ECCM using phase-perturbed LFM chirp signals and DRFM repeat jammer penalization," *IEEE Trans. Aerosp. Electron. Syst.*, vol. 42, no. 1, pp. 191–205, Jan. 2006.
- [20] W. Li, X. Lu, X. Da, and D. Liang, "Antijamming method based on orthogonal codes jittered and random initial phase for SAR," in *Proc. IET Int. Conf. Radar Syst. (Radar)*, Edinburgh, U.K., Oct. 2007, pp. 1–5.
- [21] Q. Feng, H. Xu, Z. Wu, and B. Sun, "Deceptive jamming suppression for SAR based on time-varying initial phase," in *Proc. IEEE Int. Geosci. Remote Sens. Symp. (IGARSS)*, Beijing, China, Jul. 2016, pp. 4996–4999.
- [22] M. A. Hossain, I. Elshafiey, M. A. Alkanhal, and A. Mabrouk, "Anti-jamming capabilities of UWB-OFDM SAR," in *Proc. Eur. Radar Conf. (EuRAD)*, Manchester, U.K., 2011, pp. 313–316.
- [23] S. C. Luo, Y. Xiong, H. Cheng, and B. Tang, "An algorithm of radar deception jamming suppression based on blind signal separation," in *Proc. Int. Conf. Comput. Problem-Solving (ICCP)*, Chengdu, China, Oct. 2011, pp. 167–170.
- [24] B. Zhao, L. Huang, C. He, C. Guo, J. Zhang, and J. Wang, "SAR deception jamming identification via differential feature enhancement," in *Proc. CIE Int. Conf. Radar (CIE ICR)*, Guangzhou, China, 2016, pp. 1–5.
- [25] B. Zhao, L. Huang, and J. Zhang, "Single channel SAR deception jamming suppression via dynamic aperture processing," *IEEE Sensors J.*, vol. 17, no. 13, pp. 4225–4230, Jul. 2017.
- [26] J. Högbom, "Aperture synthesis with a non-regular distribution of interferometer baselines," *Astron. Astrophys. Suppl. Ser.*, vol. 15, pp. 417–426, Jun. 1974.
- [27] H. Ghaemi, M. Galletti, T. Boerner, F. Gekat, and M. Viberg, "CLEAN technique in strip-map SAR for high-quality imaging," in *Proc. IEEE Aerosp. Conf. (AeroConf)*, Big Sky, MT, USA, Mar. 2009, pp. 1–7.
- [28] Z. Zhu, G. Tang, P. Setlur, S. Gogineni, M. B. Wakin, and M. Rangaswamy, "Super-resolution in SAR imaging: Analysis with the atomic norm," in *Proc. IEEE Sensor Array Multichannel Signal Process. Workshop (SAM)*, Piscataway, NJ, USA, Jul. 2016, pp. 1–5.
- [29] I. G. Cumming and H. C. Wong, *Digital Processing of Synthetic Aperture Radar Data: Algorithms and Implementation*. Norwood, MA, USA: Artech House, 2005.
- [30] B. Zhao, F. Zhou, M. L. Tao, Z. J. Zhang, and Z. Bao, "Improved method for synthetic aperture radar scattered wave deception jamming," *IET Radar, Sonar Navigat.*, vol. 8, no. 8, pp. 971–976, Oct. 2014.
- [31] A. M. Bruckstein, D. L. Donoho, and M. Elad, "From sparse solutions of systems of equations to sparse modeling of signals and images," *SIAM Rev.*, vol. 51, no. 1, pp. 34–81, 2009.
- [32] M. Elad, J.-L. Starck, P. Querre, and D. L. Donoho, "Simultaneous cartoon and texture image inpainting using morphological component analysis (MCA)," *Appl. Comput. Harmon. Anal.*, vol. 19, no. 3, pp. 340–358, 2005.
- [33] A. Belloni, V. Chernozhukov, and L. Wang, "Square-Root LASSO: Pivotal recovery of sparse signals via conic programming," *Biometrika*, vol. 98, no. 4, pp. 791–806, 2011.
- [34] P. Babu and P. Stoica, "Connection between SPICE and Square-Root LASSO for sparse parameter estimation," *Signal Process.*, vol. 95, pp. 10–14, Feb. 2014.

- [35] M. Grant, S. Boyd, and Y. Ye. (2016). *CVX: MATLAB Software for Disciplined Convex Programming*. [Online]. Available: <http://cvxr.com/cvx/>
- [36] *MSTAR Public Dataset*. Accessed: Oct. 10, 2016. [Online]. Available: <https://www.sdms.afrl.af.mil/index.php?collection=mstar/>



Bo Zhao (M'15) was born in Henan, China, in 1986. He received the B.Sc. and Ph.D. degrees from Xidian University, Xi'an, China, in 2010 and 2015, respectively.

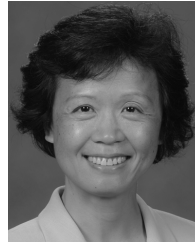
He is currently a Post-Doctoral Researcher with the Institute of Multi-Dimensional Signal Processing, Shenzhen University, Shenzhen, China. His research interests include radar imaging, synthetic aperture radar countermeasures, and compressive sensing.



Lei Huang (M'07–SM'14) was born in Guangdong, China. He received the B.Sc., M.Sc., and Ph.D. degrees in electronic engineering from Xidian University, Xi'an, China, in 2000, 2003, and 2005, respectively.

From 2005 to 2006, he was a Research Associate with the Department of Electrical and Computer Engineering, Duke University, Durham, NC, USA. From 2009 to 2010, he was a Research Fellow with the Department of Electronic Engineering, City University of Hong Kong, Hong Kong, and a Research Associate with the Department of Electronic Engineering, The Chinese University of Hong Kong, Hong Kong. From 2011 to 2014, he was a Professor with the Department of Electronic and Information Engineering, Shenzhen Graduate School, Harbin Institute of Technology, Harbin, China. Since 2014, he has been with the Department of Information Engineering, Shenzhen University, Shenzhen, China, where he is currently a Distinguished Professor. His research interests include spectral estimation, array signal processing, statistical signal processing, and their applications in radar, navigation, and wireless communications.

Dr. Huang has been on the editorial board of the IEEE TRANSACTIONS ON SIGNAL PROCESSING since 2014 and *Digital Signal Processing* (Elsevier) since 2012. He is also an Elected Member of the Sensor Array and Multichannel Technical Committee of the IEEE Signal Processing Society.



Jian Li (S'87–M'91–SM'97–F'05) received the M.Sc. and Ph.D. degrees in electrical engineering from The Ohio State University, Columbus, OH, USA, in 1987 and 1991, respectively.

She is currently a Professor with the Department of Electrical and Computer Engineering, University of Florida, Gainesville, FL, USA. Her publications include *Robust Adaptive Beamforming* (Wiley, 2005), *Spectral Analysis of Signals: The Missing Data Case* (Morgan & Claypool, 2005), *MIMO Radar Signal Processing* (Wiley, 2009), and *Waveform Design for Active Sensing Systems—A Computational Approach* (Cambridge University Press, 2011). Her research interests include spectral estimation, statistical, and array signal processing, and their applications to radar, sonar, and biomedical engineering.

Dr. Li is a fellow of the IET. She was a member of the editorial board of *Signal Processing*, a publication of the European Association for Signal Processing, from 2005 to 2007, and the IEEE SIGNAL PROCESSING MAGAZINE from 2010 to 2012. She is currently a member of the Sensor Array and Multichannel Technical Committee of the IEEE Signal Processing Society. She has co-authored the paper that has received the M. Barry Carlton Award for the best paper published in the IEEE TRANSACTIONS ON AEROSPACE AND ELECTRONIC SYSTEMS in 2005. She has also co-authored a paper published in the IEEE TRANSACTIONS ON SIGNAL PROCESSING that has received the Best Paper Award in 2013 from the IEEE Signal Processing Society. She received the 1994 National Science Foundation Young Investigator Award and the 1996 Office of Naval Research Young Investigator Award. She was an Executive Committee Member of the 2002 International Conference on Acoustics, Speech, and Signal Processing, Orlando, FL, USA, in 2002. She was an Associate Editor of the IEEE TRANSACTIONS ON SIGNAL PROCESSING from 1999 to 2005 and the IEEE SIGNAL PROCESSING MAGAZINE from 2003 to 2005.



Peichang Zhang (M'15) received the B.Eng. degree (Hons.) in electronic engineering from the University of Central Lancashire, Preston, U.K., in 2009, and the M.Sc. and Ph.D. degrees in wireless communications from the University of Southampton, Southampton, U.K., in 2010 and 2015, respectively.

He is currently with the College of Information and Engineering, Shenzhen University, Shenzhen, China. His research interests include radar signal processing, antenna selection, coherent and non-coherent detection, iterative detection, and channel estimation.